2018

BNL 50460

2[illegible]
1-28-76
NRC-8

HTGR SAFETY EVALUATION DIVISION

QUARTERLY REPORT
April 1, 1975 to June 30, 1975

NOTICE

PORTIONS OF THIS REPORT ARE ILLEGIBLE. It has been reproduced from the best available copy to permit the broadest possible availability.

DEPARTMENT OF APPLIED SCIENCE

MASTER

BROOKHAVEN NATIONAL LABORATORY

ASSOCIATED UNIVERSITIES, INC.

UNDER CONTRACT NO. E(30-1)-16 WITH THE

UNITED STATES ENERGY RESEARCH AND DEVELOPMENT ADMINISTRATION

BNL 50460
(Advanced Reactor Safety Research,
Gas Cooled Reactors - NRC-8)

HTGR SAFETY EVALUATION DIVISION

QUARTERLY REPORT
April 1, 1975 to June 30, 1975

NOTICE

PORTIONS OF THIS REPORT ARE ILLEGIBLE. It has been reproduced from the best available copy to permit the broadest possible availability.

DONALD G. SCHWEITZER, Head
HTGR Safety Evaluation Division

The High Temperature Gas Cooled Reactor (HTGR) Safety Evaluation Division provides research and analytical support to the Nuclear Regulatory Commission (NRC) - Office of Nuclear Regulatory Research (RSR) on all aspects of HTGR's regarding public safety. In addition to BNL personnel, the HTGR Safety Evaluation Division uses a wide national and international base of consulting expertise for RSR by close collaboration with consultants and subcontractors at universities and scientific establishments.

This work was performed under the auspices of the Nuclear Regulatory Commission Contract No. E(30-1)-16.

BROOKHAVEN NATIONAL LABORATORY
UPTON, NEW YORK 11973

DISTRIBUTION OF THIS DOCUMENT IS UNLIMITED

NOTICE

Printed in the United States of America
Available from
National Technical Information Service
U.S. Department of Commerce
5285 Port Royal Road
Springfield, VA 22161
Price: Printed Copy $7.00 (on foreign purchases, add $2.50);
Microfiche $2.25

November 1975 365 copies

TABLE OF CONTENTS

Summary

Cesium to be used in the thermodynamic and desorption rate studies on H451 graphite has been prepared for irradiation in the BNL medical reactor and the apparatus is near completion. Calculations of thermodynamic functions of carbonyl iodide have been made and compared with other halide carbonyls.

Initial measurements of the oxidation of graphite in air and wet helium have been carried out. The influence of impurities, types of graphite and variations in a given batch of graphite were found to markedly vary the rates of oxidation.

The Helium Impurities Loop is near completion and startup is expected by August 31. The loop, which is capable of achieving a velocity up to 150 ft/sec, will be used to test several grades of graphite in three tubes each about 2" inside diameter and 20" long. The specimens proposed will be 1/4" and 1/2" diameter tensile-type cylinders. In addition to these specimens, metal and graphite corrosion tabs will be exposed. The post-operation examination program will involve oxidation rate measurements, tensile strength measurements, metallography, chemistry (impurities in graphite) and non-destructive testing. A gas chromatograph, which was obtained through another program, is presently being modified for use with the loop.

Two large sections of ATJ and PGX graphites have been sectioned into smaller pieces for use in the chemistry and corrosion programs. The first series of samples will be taken from the ATJ graphite.

Samples will be analyzed for Fe, Si, Al, Ca, Mg, Ti, V, Ni and Mn by the emission spectrographic method. The purpose of this work is to develop analytical data required to determine the impurity distribution profile of a typical ATJ graphite post and to correlate this data with oxidation and strength measurements.

The review and assessment of the state of the art is continuing in the areas of metals, graphite and concrete. Equipment is being set up for studies on creep, creep rupture, high cycle fatigue, low cycle fatigue and tensile properties of metals in the HTGR environment. High cycle fatigue tests on Incoloy 800 in air at 1200 and 1400°F are under way. Tests under full alternating stresses and under tension mean loads are being performed. Microstructures and fracture morphology of HTGR graphites are being studied at the Aerospace Corporation using the scanning electron microscope.

Data on concrete pertaining to compressive strength, modulus of elasticity, flexural strength, shrinkage, and creep were reviewed. The limited data available indicate a deleterious effect of free water in heated concrete on the properties of the concrete. The rate of creep increases, strength decreases, and shrinkage strains increase.

A review of the analytical and numerical techniques to evaluate the PCRV structural integrity was carried out. The investigation indicates that the existing computer methods are only valid for normal operations and slight over-pressure excursions. Their application to accident conditions, such as those resulting in high overpressures, liner cooling pipe failures, gross or spot overheating of the concrete, is limited by certain theoretical and material considerations. Extension of the numerical techniques to account for accident conditions of the type mentioned above have been initiated.

Recent studies demonstrate that crack propagation rate, crack orientation, and critical crack size in metals are dependent on the bi-axial stress ratios of the structure. For the liner this type of behavior can be critical especially for those areas where the vessel liner intersects the penetration liner.

The development of computer codes for seismic analysis continues. The horizontal array computer code has been completed and tested and will soon be released together with a user's manuel. A parametric study is presently being completed.

The GOPTWO computer program was used extensively during the quarter to study the effect of water vapor depletion during passage through an HTGR core. It was found that over a wide range of steam ingress rates and near the upper limit of the graphite-steam reaction rate, the steady state water vapor concentration in the lower plenum did not differ appreciably from that in the upper plenum. It was also found that the water vapor concentration follows a simple exponential relationship to the ingress rate.

The GA Univac 1108 version of the OXIDE3 code has been converted to run on the BNL CDC 7600. The conversion has been verified by a comparison of output obtained from both machines for the same sample problem. An automatic time step feature was introduced into OXIDE3 to facilitate steady state calculations for various parameter sensitivity studies; e.g., core coolant impurity gas concentrations resulting from various fixed steam leak rates. A preliminary comparison of the latter calculations with results from GOPTWO agreed to within 20%.

The computer model of the HTGR helium circulator-steam turbine was made into a module that can be incorporated into other systems codes. This module has been sent to ORNL for inclusion in their modeling effort on HTGR systems dynamics.

The TFR (Two Fluid Relap) systems code was tested under limited boundary conditions that do not yet include the steam generator characteristics. Simultaneous reactor power and turbo-compressor steam pressure/flow ramp-down situations have been modeled and appear to have executed properly.

I. Fission Product Release and Transport (H. Isaacs)

A. Brooklyn College Subcontract (R. Behrens and S. Aronson)

Work continues in establishing an experimental program to study desorption rates and desorption thermodynamics of fission metals sorbed on reference H-451 graphite. The initial work will involve a study of cesium.

Concurrent with the experimental program, estimation and evaluation of thermochemical data for gaseous molecules of possible importance in establishing fission product release from HTGR cores will continue.

Approximately 300 mg of 99.98% pure elemental cesium sealed in an evacuated ($< 10^{-5}$ torr) quartz tube have been submitted for irradiation in the BNL medical reactor. The intent is to produce approximately 0.1 mCi of the gamma emitter Cs-134 for use as a radiotracer in Knudsen effusion measurements of the vapor pressure of elemental cesium. The reasons for this study prior to the cesium-graphite desorption studies are two-fold:

1. To determine systematic errors present in the effusion cell temperature measurements and in the scintillation pulse counting measurements.

2. To study an apparent discrepancy in the vapor pressure, enthalpy, and entropy of vaporization of liquid cesium.(1-1) High temperature static measurements yield vapor pressures somewhat discordant with values obtained from static measurements at low temperature. The vapor pressure of cesium apparently has not been measured

using the Knudsen effusion technique and, as such, our measurements would provide needed confirmation of the vapor pressure and thermodynamic properties of vaporization.

For various reasons a homemade furnace has proven unsatisfactory for our use and, therefore, a Mellen split tube furnace capable of achieving 1200°C has been acquired. However, there have been problems supplying power to the furnace from a two position proportional controller. It is expected to have this problem solved shortly.

The position of the thermocouple feedthrough arrangement has been changed in order to reduce the length of thermocouple wire needed within the vacuum system and to permit the thermocouple to be routinely removed from the vacuum system for calibration.

Two FORTRAN IV computer programs for calculating thermodynamic functions of gaseous molecules have been put into use. Programs LIN and NONLIN compute heat capacities, entropies, enthalpies, and free energy functions for linear and nonlinear molecules respectively using the rigid-rotator, harmonic oscillator approximation. Brief program descriptions and card input formats for these programs have been supplied to BNL as well as a description of the thermal data fitting and thermal function generation program FITAB referred to in our previous report.

Thermodynamic functions for carbonyl iodide, $COI_2(g)$, have been computed using structural parameters and fundamental vibrational wave numbers estimated from trends in known values for $COH_2(g)$ and other carbonyl halides.

Principal moments of inertia used in these calculations are computed to be I_A = 844, I_B = 940, and I_C = 95 amu-$\mathring{A}^2$ from estimated values of 2.2Å and 1.1Å for the C-I and C=O bond lengths and 112° for the I-C-I bond angle.

Being a tetra-atomic non-linear molecule with symmetry of point group C_{2v}, $COI_2(g)$ has six singly degenerate fundamental vibrational wave numbers. They are estimated to be: ν_1 = 1782, ν_2 = 332, ν_3 = 134, ν_4 = 532, ν_5 = 292, and ν_6 = 439 cm^{-1}.

Standard thermodynamic functions for $COI_2(g)$ are presented in Table 1-1. The value of S^o_{298} = 78.07 cal K^{-1} $mole^{-1}$ may be compared with S^o_{298} = 61.84, 67.82, and 73.82 cal K^{-1} $mole^{-1}$ for $COF_2(g)$(1-2), $COCl_2(g)$(1-2), and $COBr_2(g)$(1-3) respectively.

The enthalpy of formation, $\Delta H^o_f(0^oK)$ for $COI_2(g)$ is estimated to be -5 kcal $mole^{-1}$ from values of $\Delta H^o_f(0^oK)$ for C(g), I(g), and O(g) given by Hultgren _et al_,(1-1) and average bond energies for the C=O(1-4) and C-I(1-5) bonds.

$\Delta H^o_f(298)$, $\Delta S^o_f(298)$, and $\Delta G^o_f(298)$ are computed to be -6.0 kcal $mole^{-1}$, -24.50 cal K^{-1} $mole^{-1}$ and -13.29 kcal $mole^{-1}$ respectively using values of $(H^o_{298} - H^o_o)$ and S^o_{298} for $COI_2(g)$ in Table 1-1 and for the elements in Hultgren _et al_.(1-1)

Table 1-1 Standard Thermodynamic Functions for Carbonyl Iodide, $COI_2(g)$.

(^oK)	C_P (cal K^{-1} mole^{-1})	$H^o_T - H^o_{298}$ (a) (cal mole^{-1})	S^o_T (cal K^{-1} mole^{-1})	$-(G^o_T - H^o_{298})/T$ (cal K^{-1} mole^{-1})
298.15	15.76	0.	78.073	78.073
400	16.71	1658.	82.850	78.705
500	17.33	3361.	86.649	79.926
600	17.78	5118.	89.850	81.320
700	18.14	6915.	92.619	82.741
800	18.43	8744.	95.061	84.131
900	18.65	10598.	97.245	85.469
1000	18.83	12473.	99.220	86.747
1100	18.98	14364.	101.022	87.964
1200	19.10	16268.	102.679	89.122
1300	19.20	18183.	104.212	90.225
1400	19.28	20107.	105.638	91.275
1500	19.35	22038.	106.970	92.278

(a) $H^o_{298} - H^o_0 = 3600.$ cal mole^{-1}.

References

1-1. R. Hultgren, P. D. Desai, D. T. Hawkins, M. Gleiser, K. K. Kelley and D. D. Wagman, Selected Values of the Thermodynamic Properties of the Elements, ASMT, Metals Park, Ohio (1973).

1-2. D. R. Stull, I. Carr, J. Chao, T. E. Dergazarian, L. A. duPlessis, R. E. Jostad, S. Levine, F. L. Oetting, R. V. Petrella, H. Prophet, and G. C. Sinke, JANAF Thermochemical Tables, Clearinghouse for Federal Scientific and Technical Information, Springfield, Va. (1966).

1-3. J. Overend and J. C. Evans, Trans. Faraday Soc. 55, 1817 (1959).

1-4. George J. Janz, Thermodynamic Properties of Organic Compounds, Academic Press, N. Y. (1967).

1-5. J. A. Kerr and A. F. Trotman-Dickenson in Handbook of Chemistry and Physics, The Chemical Rubber Co., 51st Ed., 1970-1971, p. F-164.

II. Primary Coolant Impurities

A. Helium Impurities Loop (A. Romano)

The Helium Impurities Loop (HIL) has been assembled, welded, and leak tested, and is presently being electrically wired with heaters, thermocouples, and control instrumentation. The anticipated start of room temperature operations for shake down of equipment will be about July 1, and final operating conditions should be achieved by about August 1. The detailed design and operating conditions of the loop have been given earlier.(2-1) A review of the capabilities of the HIL is given in Table 2-1 and a schematic drawing is shown in Figure 2-1.

There are basically three modes of operation that can be attempted with the HIL. First, tests of very long duration (>10,000 hours) at normal HTGR operating conditions (low impurity levels) can be run to determine the long term effects on materials. A second mode would be to operate at accelerated conditions (high temperature, high impurity levels, etc.) for short periods of time to evaluate the effects of transients on materials and impurity monitors. Still another mode would be a combination of the aforementioned two, namely to determine the effects of short term transients on pre-exposed materials. The latter mode would be the most desirable since it will simulate actual anticipated occurrences.

Since the loop has been fabricated from materials and components which were on hand at BNL, its operational reliability for >10,000 hour runs is in doubt. It is therefore recommended that a second loop be designed and constructed for this purpose and that HIL be used for

Table 2-1

Design Operating Conditions of the Helium Impurities Loop

Gas Pump Supply:	850 liters/min (30 cfm) 13.79 K Pa (2 psig) 366^{o}K (200^{o}F)
Graphite Vessel:	2.63 Kg/hr (5.8 lbs/hr) 653^{o}K Inlet 1123^{o}K Outlet
Bypass Heater:	2.63 Kg/hr (5.8 lbs/hr) 366^{o}K Inlet 1033^{o}K Outlet
Purification System:	10 to 20% of main flow
Pump Bypass:	≈ 50% of main flow

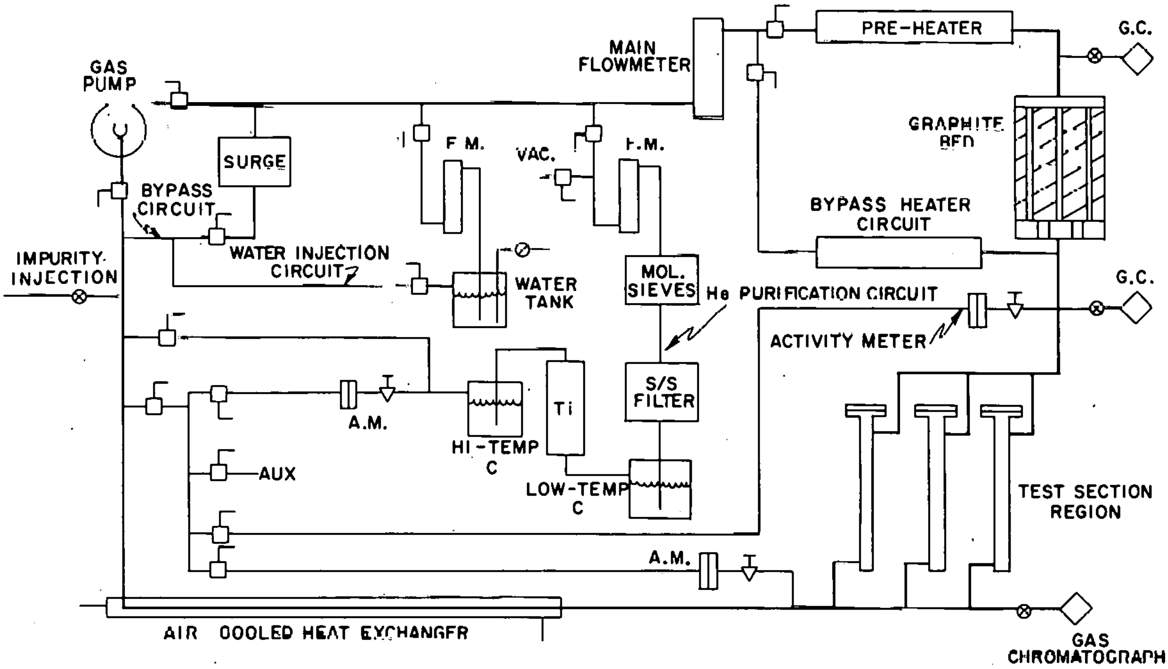

Figure 2-1. Helium impurities loop
(schematic flow sheet).

transient testing. The new loop could be fabricated from new equipment which would have the higher operational reliability required for low impurity level operation. The HIL design offers a unique advantage which should be utilized in its operation; the gas circulating pump used can supply a large volume of He (at low pressure) with the capability of achieving a very high velocity (~180 ft/sec) in the test section.

The HIL test section region consists of three vertical parallel tubes each of which is approximately 2" inside diameter and 20" long. A high-temperature (metal seal) flange at the top of each tube permits easy access to the specimens located below.

The test specimens for the first series of tests will be made from candidate HTGR graphites:

H451	core graphite
ATJ	core support posts
PGX	core support blocks

The specimens will be 1/4" diameter x 3" long and 1/2" diameter x 6" long. Each specimen will be fixed to the end of an adjacent specimen to form a column approximately 18"-21" long. Several columns, supported at top and bottom, can be installed in each test section tube. The first series of tests will be screening tests to confirm earlier observations, determine the effects of surface/volume ratio, and establish a relative comparison of the graphites tested. Some of the specimens will be doped with additional impurities. Observations will be based on the following measurements performed on the specimens:

1. Oxidation rate - ΔW, area, time, temperature, BET surface.
2. Mechanical strength - tensile, crack propagation.
3. Metallography - optical, scanning electron microscope.
4. Chemistry - metallic impurities.
5. Non-destructive testing - sonic velocity measurements.

A second series of tests, using the graphites listed above, will be performed on larger specimens to determine the effect of velocity on the oxidation rate. The test section will be designed to provide velocities over the graphite surfaces of from 25 to 150 ft/sec. Specimens ranging from 1.0" to 1.8" in diameter will be exposed.

The HIL has been provided with several ways of introducing impurities and a purification circuit for controlling the impurity concentration of the He. Impurities can be introduced by directly injecting the particular specie(s) of interest or by reacting water vapor with a large block of graphite located upstream of the test specimens. Control of the concentration can be achieved by blending purified He with the less pure He in the main circuit.

A gas chromatograph, which was made available from another research program, will be used to monitor the He stream at several points around the loop. The chromatograph will have the capability of measuring H_2, CO, CO_2, CH_4, O_2, and N_2 using up to six columns and three detectors (thermal conductivity). A dew point meter will be used to monitor H_2O concentration. Other instruments, i.e., a new gas chromatograph, the mass spectrometer to be installed in the Fort St. Vrain HTGR, etc. will eventually be tested in HIL and will be compared to other instruments including several electrochemical oxygen meters under construction.

The impurity concentration of the loop will be maintained at 50 times the equivalent HTGR level of interest (ratio of He pressures between HIL and HTGR). Since the present GA Technical Specification limit for total oxidants in an HTGR is $<$ 3000 ppm-days, $< 1.5 \times 10^5$ ppm-days will be the corresponding limit for comparison in our tests. Therefore, the following table will be used as a guide in our test program:

Desired HTGR Condition for Comparison 3000 ppm-days	HIL Operating Level 1.5×10^5 ppm-days
$<$ 10 ppm (normal level)	$<$ 500 ppm
10^2 to 10^3 ppm (transients)	5×10^3 to 5×10^4

B. Impurity Monitoring (H. Isaacs)

A number of electrochemical cells have been constructed and tested. The cell design is a carryover from an earlier program where cell operation was at 500°C. The cells being used for determining the total oxygen in helium are operated at 750°C and a not unexpected problem has arisen with the use of o-rings which apparently leak at the higher temperature.

Potentials of up to 800 mV have been recorded with air as the reference gas and graphite in contact with the inner compartment. This value is in the range expected from calculations. In one cell a marked gas flow rate was observed which may have been caused by a leakage path between the inside and outside of the cell, or may have resulted from a slow reaction rate of the catalyzed graphite and impurities in the gas stream. Calculations are at present in progress which analyze the potential changes, in terms of the reaction rate of water with graphite, as a function of the changes in the composition of the gas. This work will probably offer a rapid technique for the determination of graphite oxidation as a function of water, CO and hydrogen concentration.

III. Rapid Graphite Oxidation

A. Analysis of Impurities in Graphite (A. Romano)

Two large sections of candidate HTGR core support graphites (ATJ and PGX) have been received from Union Carbide Company for use in our experimental program. The graphites will be used to supply specimens for chemical analysis, oxidation rate measurements, metallographic studies, physical property measurements, and mechanical testing.

The ATJ graphite is representative of that used in the Ft. St. Vrain core support system. The 8" x 17" x 52" log was split longitudinally by Union Carbide Company in order to form the shapes used to fabricate two posts. One of these shapes will be used for the chemical analysis program while the other will be used for the other programs. Similarly, a 500 lb section of PGX core support graphite was received. Portions of the block will be set aside for future chemical analysis.

The purpose of the chemistry program is to develop the analytical data required to determine the impurity distribution profile of one of the ATJ graphite posts and to correlate this data with oxidation and strength measurements which will be performed on the second post. Further, an attempt will be made to establish the nature, location, and concentration of each of the catalytic species in the graphite matrix. When this is well established, a similar but limited program will be initiated on the PGX graphite.

Several analytical procedures were reviewed and evaluated, and it was concluded that emission spectroscopy would be a promising technique to employ for graphites such as ATJ and PGX (high ash contents). Several discussions with the Analytical Group and results from their preliminary analyses have led to the following conclusions:

1. Room temperature ashing, employing ionized oxygen, is practical only for nuclear grade graphites (H451). Ashing of ATJ and PGX samples (1 g) will take several days.

2. Lump samples of ATJ should be ashed at 450°C (instead of 850°C) in oxygen. This would reduce the amount of impurity loss due to volatilization. Ashed samples could then be put into acid solution and analyzed by atomic absorption.

3. Ground and powdered ATJ could be analyzed by directly arcing in the emission spectrograph. By purchasing a direct reading attachment (photomultiplier tube), this method would allow the analysis of a large number of samples in a short period of time and, compared to the other methods considered, appears to be the one most suited for the proposed task.

4. The proton-induced x-ray fluorescence method could be rapid but first requires standardization. However, the method is limited since it only analyzes a small sample of graphite and will not analyze elements under atomic number 15. This would include two of the major impurities, Al and Si. The method could be useful for qualitative surface analyses and for analyzing highly volatile elements such as S and Cl.

Evaluation of analytical methods is continuing. The Analytical Group has been informed of the new proposed ASTM test methods for analyzing impurities in graphite and will participate in chemistry round robins. Results from these evaluations will provide input for a final decision on the analytical method to be used.

A list of elements of interest in our program is given in Table 3-1. The selection of these elements was as follows:

1. Elements known to be present in ATJ graphite at levels of 1 ppm or higher.

2. Elements which have been reported to act as catalytic agents in the oxidation of graphite.

3. Elements which might be present in the reactor coolant stream, i.e. fission product impurities.

Elements which fit the combined descriptions of (1) and (2), Fe, Si, Al, Ca, Mg, Ti, V, Ni, and Mn, will be analyzed on every sample. All of the other elements listed in Table 3-1 will be randomly analyzed.

On June 3-4, 1975, A. Romano attended a meeting of an ASTM Subcommittee which was held at General Atomic Company (GA). The Subcommittee is a task group responsible to a larger committee (C5.05 Nuclear Applications of Graphite) regarding the analysis of impurities in graphite.

The task group presently consists of members representing the carbon products manufacturers, GA, HNL (ORNL) and BNL. The group is primarily interested in nuclear grade (core) graphite, boronated graphites and B_4C. Several procedures have been written and round robins have been completed or are under way (in which BNL will participate). Copies of the procedures were obtained and have been distributed to the BNL analytical people for comment.

Table 3-1

Elements of Interest in ATJ Graphite

Element	Highest Conc, ppm	Major Impurity	Known Catalyst	Fission Product	Analyze on Every Sample
Fe	400	Yes	Yes		Yes
S	400	Yes			
Si	250	Yes	?		Yes
Al	125	Yes	?		Yes
Ca	100	Yes	?		Yes
Mg	50	Yes	?		Yes
Ti	40	Yes	Yes		Yes
V	40	Yes	Yes		Yes
Ni	30	Yes	Yes		Yes
Mn	20	Yes	Yes		Yes
Co	< 5		Yes		
Ag	< 1		Yes	?	
Mo	< 1		Yes		
B	< 5		Yes		
Cs	< 1		Yes	Yes	
Ba	< 1		Yes	Yes	
Sr	< 1		Yes	Yes	
Li	< 1		Yes	?	
Pt	< 1		Yes		
Cu	< 5		?		
W	< 1		?		
Cr	< 5		?		
Pb	< 1		Yes		

B. Graphite Oxidation (H. Isaacs)

In attempting to assess the effects of impurities on graphite, there appeared to be no general understanding of the action of catalytic impurities, their concentrations, and the effect of their distribution in the graphite. As these aspects of the problem are required in predicting the safety of HTGR's, a program was initiated to study the consequences of impurities and impurity distribution on the structural integrity of graphite. The work will be in conjunction with mechanical property changes and the influence of oxidation on the mode of fracture of graphites. This report covers the initial measurements which have been conducted with graphite materials on hand and using a simple test apparatus.

Apparatus

Tests were performed in air in simple furnaces and wet helium. The apparatus for helium exposure consisted of a vertical tube 2" in diameter and 24" long with helium entering at the bottom and leaving near the top. Water additions were made by saturating the helium by bubbling through water at a known temperature. Checks on water level concentrations entering and leaving the vessel were made using a dew point method. In most tests the range of helium flow rate was approximately 8 to 20 standard cc/sec depending upon the test. At these flow rates, considering that the supply helium was saturated with water at room temperature (23 ± 2°C), approximately 0.6 to 1.4 g/H_2O/hr was delivered to the test specimens. At 23°C, the saturation concentration of H_2O in He is about 13 weight or 2.8 volume percent.

In one test where flow rates were low mass balances were calculated assuming an equal molar quantity of water reacted with graphite to account for all of the weight loss. These calculations provided good agreement based upon the aforementioned rates of water ingress and the measured graphite weight losses. One could conclude from these calculations that nearly all of the water was consumed on passing through the reaction vessel. This deduction is consistent with the dew point measurements and with the long contact time in vessel (~3 minutes).

When contaminated graphite samples were used the reaction rate was sufficiently high to reduce the concentration of water. Specimens located towards the exit at the upper end of the test section were exposed to unknown impurity levels and showed a decreased reaction rate.

Graphite Samples

H451 graphite, directly related to the HTGR program, had a total ash of 33 ppm and a density of nominally 1.76 g/cm^3; the measured density was 1.73 g/cm^3. The other graphites used were obtained from a stored supply of materials and were up to 20 years old. The designations of these graphites, their densities, and original size, are given in Table 3-2.

Controls from the 1" x 1" x 24" (A) graphite specimens taken

Table 3-2

Types, Properties and Ash Content of Graphites Tested

Original Size	Designation	Density	Ash ppm
Cylinder 17½" diameter	H451 (H451)$^+$	1.73	36
1" x 1" x 24"	AGHT* (A)$^+$	1.72	70
4" x 4" x 24"	AGHT* (B)$^+$	1.69	~100
Plates 3 to 10mm thick	? (Plate)$^+$	1.61	2700

*Possible designation
+Text reference

from the top and center, respectively, of the storage container were qualitatively analyzed by the proton induced x-ray fluorescence method to determine major differences in impurities. The technique can analyze a 2 mm spot size only to a depth of 0.2 mm. Thus the results would be indicative of only those impurities on the surface. The results were as follows:

Ratio of $\left\{\frac{\text{Sample from top of container}}{\text{Sample from center of container}}\right\}$	Element
100	Pb
6	Fe
12	Ca
≤ 1	S,V,K,Ti,Cu,Zr

The contaminants Pb, Fe, Ca are clearly among those which could have settled from the atmosphere during storage. In order to gain a more definite characterization of the graphites used in these tests, samples were analyzed for total ash content. These results are reported in Table 3-2. "Type CS" graphite, with a total ash content of 80 to 135 ppm, is of nuclear grade. The major impurities reported are: 50 ppm Cu, 10 ppm Fe, 10 ppm Ni, ≤1 ppm each of Mg, Mn, Pb, Cr, Al, Ca and between 30 and 100 ppm Si. The uncertainty in the Si concentration arises from the possibility of contamination by silicone grease used in the low temperature ashing apparatus.

Impurities and Impurity Impregnation of Graphite

Various forms of iron were used to contaminate graphite samples to investigate the effects of impurity distributions. Qualitative effects were sought to survey these effects. The solutions used were:

1. Ferric Chloride - a solution of 10% $FeCl_3 \cdot 6H_2O$ was

prepared.

2. Iron Powder - this mixture consisted of iron powder ("reduced electrolytic iron") suspended in solution by agitation just prior to impregnating the graphite.
3. Ferric Hydroxide Solution - this suspension was prepared by exposing mild steel to water with air agitation.

Experimental

A wide range of preliminary tests have been carried out. The tests included different types of graphite, variations within each type, and effects of time, temperature, contaminants and environments. The results are presented for each of the two environments, air and wet helium.

(a) Air Oxidation

Oxidation of the plate graphite from 570 to 650°C showed that it had a high level of impurity and high weight losses. For example, at 650° the rate varied from about 11 to 25 mg/cm^2-hr for burnoff values of 3 to 10 w/o respectively. At 570°C the rate decreased to about 1 mg/cm^2-hr.

The oxidation of samples from different plates at 570°C showed marked differences in the nature of attack. Figure 3-1 shows a comparison of two large pieces about 3 x 30 x 180 mm in size after 87.5 hours. The one sample (1) showed a loss of cohesion and crumbled after being weighed. This sample had an average rate of weight loss of 1.34 while (2) showed 0.90 mg/cm^2-hr for the 87.5 hour exposure. Both samples showed pits which penetrated through the thickness, with

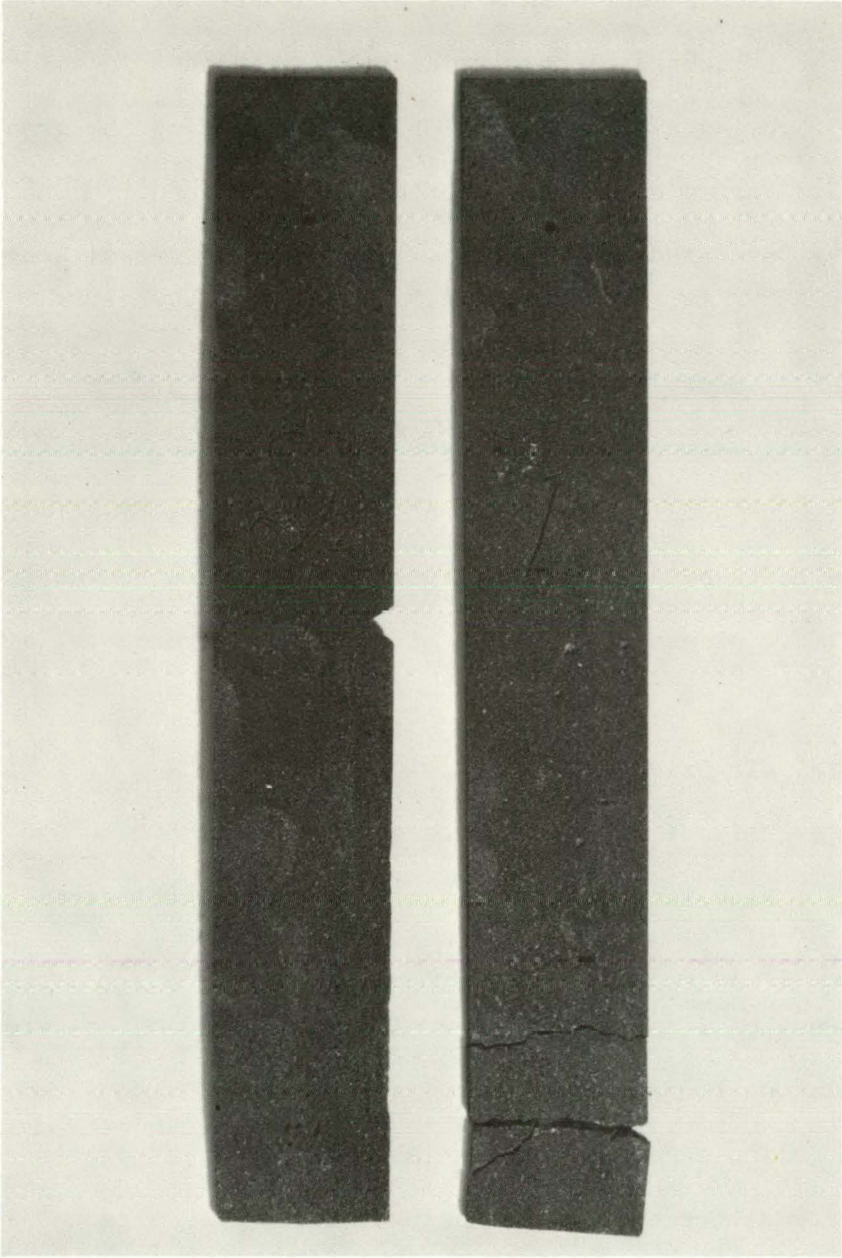

Figure 3-1.

more pits being found on sample (1). Within many, but not all, of the pits was a rust colored powder with iron as a major component as indicated by electron microprobe analysis. High concentrations of impurities (2700 ppm) were shown by ashing the plate graphite.

In comparison to the high weight changes of the plate graphite, (B) graphite samples 5 mm thick gave oxidation rates of 0.32 mg/cm^2-hr in comparison to a similarly exposed plate graphite rate of 1.4 mg/cm^2-hr. The exposure times were 28.5 hours at 570°C.

The effect of impurities on (B) graphite were studied with all three contaminants and 50.8 mm cubes at 650°C for 16 hours. The rates of weight loss are shown in Table 3-3, and the specimens after exposure are shown in Figure 3-2. (The samples were placed in contact for photography. They were well separated during testing and supported on a ceramic base.) The effects are apparent from the Figure. The remains of the two cubes impregnated with ferric chloride are shown on the bottom left and right. These samples lost about 75% of their initial weight compared with about 4% for the uncontaminated specimen. The contaminant which led to the second fastest rate increase was low concentrations of $Fe(OH)_3$. The higher $Fe(OH)_3$ concentration solution led to hydroxide coating on the specimen which remained on the surface when the "solution" back filled after evacuation. After oxidation the oxide formed was definitely protective to the underlying graphite.

(A) graphite was also tested in air. The first unusual behavior was noted when two specimens were placed in contact in a small furnace with a diameter slightly larger than the diagonal on

Table 3-3

Effect of Contaminants on the Rates of Oxidation of B-Type (AGHT) Graphite at 650^o in Air

Specimen No.	Contaminant	Rate of Weight Loss mg/cm^2hr	% per hr
1	low $Fe(OH)_3$	15.21	1.01
2	low $Fe(OH)_3$	27.10	1.80
3	$FeCl_3$	71.12	4.73
4	$FeCl_3$	67.29	4.48
5	Fe	14.92	0.99
6	Fe	14.76	0.98
7	$Fe(OH)_3$	16.76	1.11
8	$Fe(OH)_3$	12.16	0.81
9	None	3.93	0.26
10	None	3.47	0.23

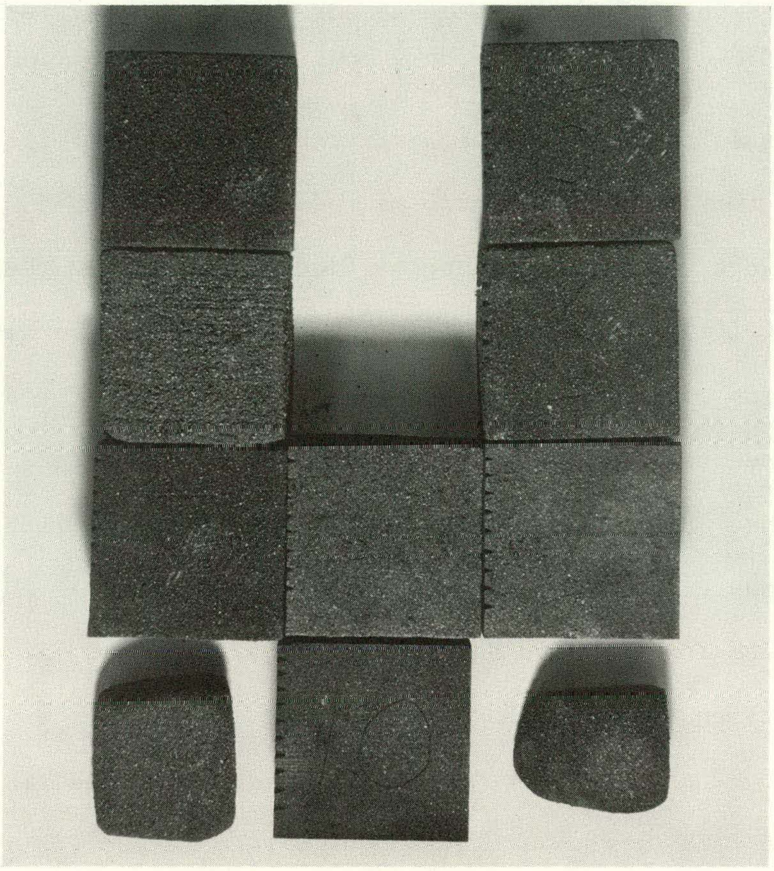

Figure 3-2.

the 1" square surface of the cube specimens. Figure 3-3 shows the two specimens after testing 18 hours at 650°C. The smaller piece that remained had lost 96% of its original weight. The lower specimen lost 37.7% in weight or 15.3 mg/cm^2-hr. Reasons for the differences could possibly be related to air and CO flow patterns in narrow furnaces but the more probable explanation is that they arise from variations in the chemical properties of the graphite itself.

Two 25 x 25 x 610 mm rods (numbered 1 and 2) of (A) graphite were cut into 11" lengths discarding 2" from the middle so that the original edges were left. The number 2 rod had been taken from the top of a container holding a large number of rods which had been exposed to the atmosphere. Number 1 rod was taken from below the surface. Rod 2 had been exposed to sources of impurities in the atmosphere such as dust and dirt. Specimens 1-A and 2-A were exposed for 22 hours and gave rates of 9.62 and 16.72 mg/cm^2-hr, while specimens 1-B and 2-B were exposed for only 6 hours and gave rates of 5.82 and 12.19 mg/cm^2-hr. In Figure 3-4 the sides of rod 2 which were face up when stored showed a very marked variation in rates with the upper surface oxidizing very rapidly and being removed after 22 hours. With rod 1, the ends of the rods which were also exposed to the atmosphere showed evidence of accelerated attack as shown in Figure 3-4. The increased rates at the ends of the rod can also be seen from another experiment conducted with a single uncut rod oxidized in air at 570°C for 15.5 hours. The rate loss for this rod was 3.82 mg/cm^2-hr. Figure 3-5(a) and 3-5(b) show the ends of the rod after exposure. The morphology of the ends was markedly

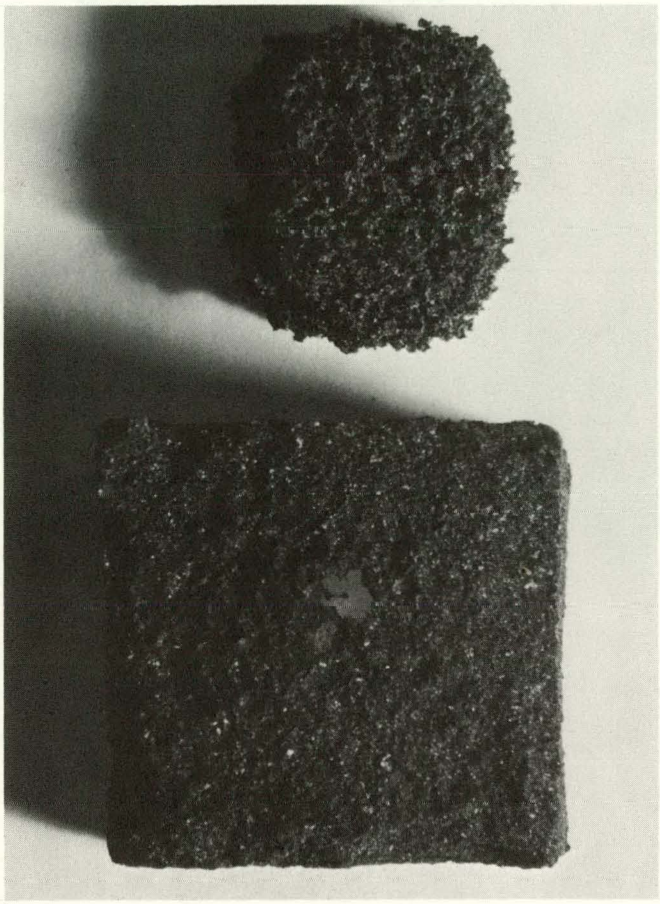

Figure 3-3.

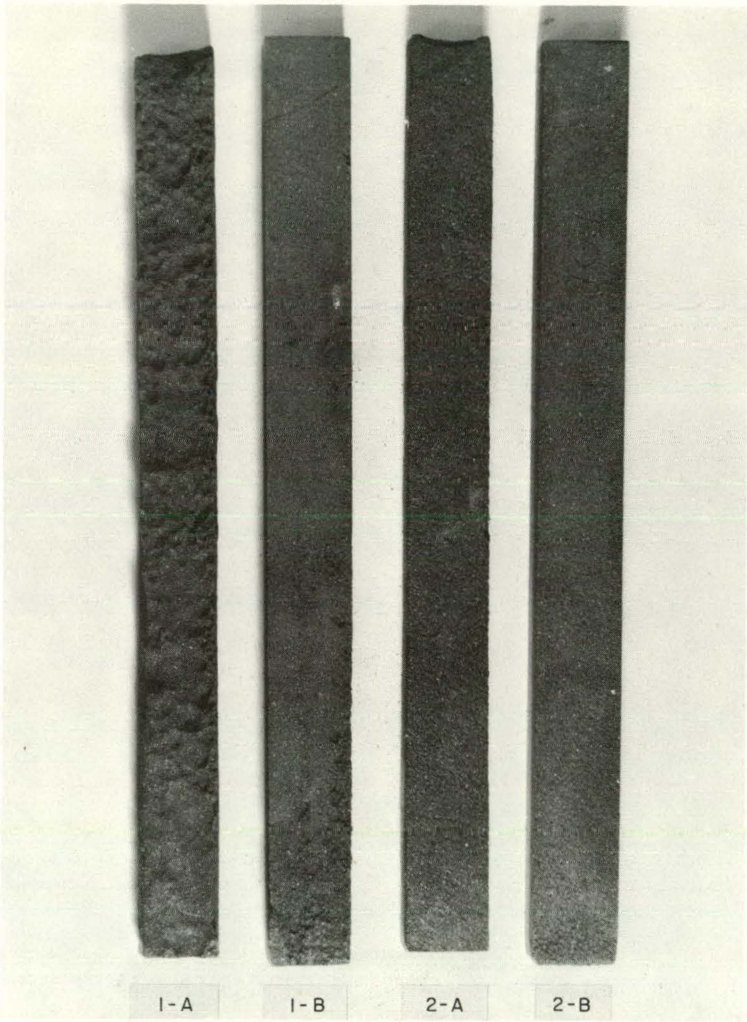

Figure 3-4.

different. Figure 3-5(a) showed a honeycomb effect with the development of a definite pore structure reminiscent of that observed with the faster oxidizing specimen shown in Figure 3-3. Figure 3-5(b) showed an attack where the structural integrity of the graphite deteriorated leaving a powdered graphite. These observations with this nominally AGHT graphite indicate the wide range of oxidation characteristics which may be observed with graphite that may be due to effects of storage, contamination or local differences.

(b) Oxidation in Helium with Water Vapor Impurity

The effect of impurities added to the graphite on its rate of oxidation was investigated in wet helium. The results using (A) graphite were markedly influenced by contamination. With no contamination added the oxidation rates were the lowest. The rates increased respectively with the following contaminants: $Fe(OH)_3$, iron powder, and ferric chloride. There was also a marked rate variation with position in the furnace due to the uptake of water and the buildup of inhibitive reaction products contaminated with ferric chloride nearest the entering helium. The other sample contaminated with ferric chloride was also oxidized to a much greater extent than adjacent samples. A problem arises with the use of ferric chloride as the salt boils at about 230°C and could be transferred to adjacent samples.

Figure 3-5a.

Figure 3-5b.

An example of the results is given for H451 graphite. The results are shown in Figure 3-6. Here once again, the effects of contamination and position were seen. In addition to the iron contamination, the effect of sodium chloride was also investigated. As shown in Figure 3-6, the salt does increase the oxidation rate but not nearly to the same extent as that caused by iron chloride. The effect of the edge of the log was also investigated but this part gave the same or lower corrosion rates as the rest of the log.

The results obtained emphasize many of the aspects of the oxidation of graphite that must be taken into account in the assessment of problems which can arise due to impurities in HTGR coolant. These aspects include flow rate, impurity level, contamination and localized oxidation differences.

The effect of sample to sample variation of (A) graphite from the same source is emphasized by Figure 3-3, and confirmed by later results, e.g. Figure 3-5. The cause of these differences is

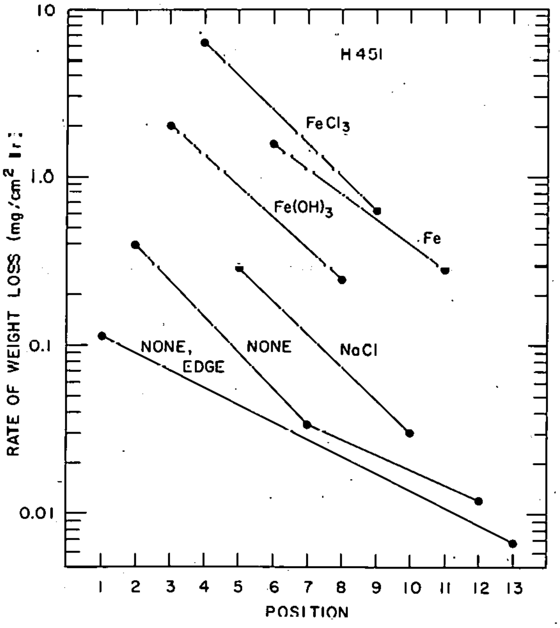
H 451
FeCl3
Fe(OH)3
Fe
NONE, EDGE
NONE
NaCl
RATE OF WEIGHT LOSS (mg/cm² hr)
10
1.0
0.1
0.01
1 2 3 4 5 6 7 8 9 10 11 12 13
POSITION

Figure 3-6.

not known with certainty but are probably a result of the contamination of the graphite during storage. The initial chemical analysis that was conducted on these samples was presented above, and showed that lead, calcium and iron were higher on the sample having an exposed surface during storage. Iron and calcium are known catalysts of graphite oxidation, but no definitive work has been carried out on lead. The other possible cause of the sample to sample differences may be inherent in the samples. This is suggested by the marked differences in the morphology of the graphite after oxidation in Figure 3-5(a) and 3-5(b). If these differences were caused by contamination then a second factor, e.g. concentration differences, or different contaminants must be present to give the morphological variations. This seems less likely. Further work will be carried out to determine the cause of these differences but not in the immediate future as emphasis will be on ATJ and PGX type graphites. The variations from sample to sample were also observed with the plate graphite. Here again different modes of attack were observed. In Figure 3-1, sample 1 lost cohesion while 2 was still resilient.

The effect of localized oxidation was very marked with the plate graphite as pits had grown completely through the specimen. Many of the pits were associated with iron impurities which could often be seen but this did not account for all the pits, and further investigation will be necessary using various contaminants.

The effect of contaminants on graphite oxidized in air indicated that the mode of addition of the impurity was important. Ferric chloride was extremely active. The effect of the hydroxide was surprising as the protection of a continuous coating on inhibiting the oxidation in air was not expected. The presence of iron particles or lower concentrations of hydroxide were more catalytic. These results also indicate that the mode and the nature of an additive is important in terms of its catalytic influence.

The effects of contaminants on the oxidation rate in wet helium can be seen from Figure 3-6 which also leads to the same conclusion as those in air. However, in this case the iron was more catalytic than that observed in air. These results also show that sodium chloride is a catalyst but the iron chloride is far more active and the chloride is not the direct cause. The effectiveness of the iron chloride may be due to either the fact that the iron will be well dispersed throughout the graphite or that an intercalation compound was formed.

The results in Figure 3-6 also show the effect of position. These results reflect the influence on the gas composition on the reaction rate. As the gas moves downstream, the hydrogen and carbon monoxide concentrations increase and act as inhibitors reducing the oxidation rate. It is interesting to note that the rate of decrease with position appears to be more rapid with the contaminated or catalyzed specimens. (Specimen with no contamination in position 2 did show some pitting which was probably caused by movement of iron chloride.) This aspect will be investigated in detail in the future as the major amount of work conducted in high purity helium has been related to nuclear or high purity graphite. Little work has been conducted on graphites with relatively high ash contents such as types

ATJ and PGX which may be used for core support posts and core support blocks. The oxidation rates and rate dependence of these graphites with different helium impurity concentrations is important in determining and extrapolating the possible changes in their mechanical properties after extended periods of time.

IV. Structural Evaluation (M. Reich, P. Bezler, J. Curreri, B. Koplik, T. Y. Chang, L. Lasker, H. Goradia, S. Trachuktam)

The work carried out by the structural analysis group during this report period for the HTGR can be categorized into the following primary areas:

PCRV and Liner
Core Seismic Response
Core and Core Support Structure

PCRV and Liner

The PCRV is a highly complex structure consisting of a concrete matrix containing steel reinforcement, prestressed tendons, and a steel liner. All of these components interact to insure the structural integrity of the system. PCRV designs were reviewed in order to evaluate the analytical and numerical techniques used for the analysis of the PCRV's. Figure 4-1 shows a schematic representation of a typical result for an axisymetric analysis that accounts for creep cracking of the concrete and plasticity of the steel liner and reinforcements. Although the method is quite advanced, the review indicated that the existing computer methods are only valid for normal operations and slight overpressure excursions. Their application to accident conditions, such as those resulting in high overpressures, liner cooling pipe failures, gross or spot overheating of the concrete, etc., is limited by certain theoretical and material considerations. Extension of the numerical techniques to account for accident conditions of the type mentioned above has recently been started.

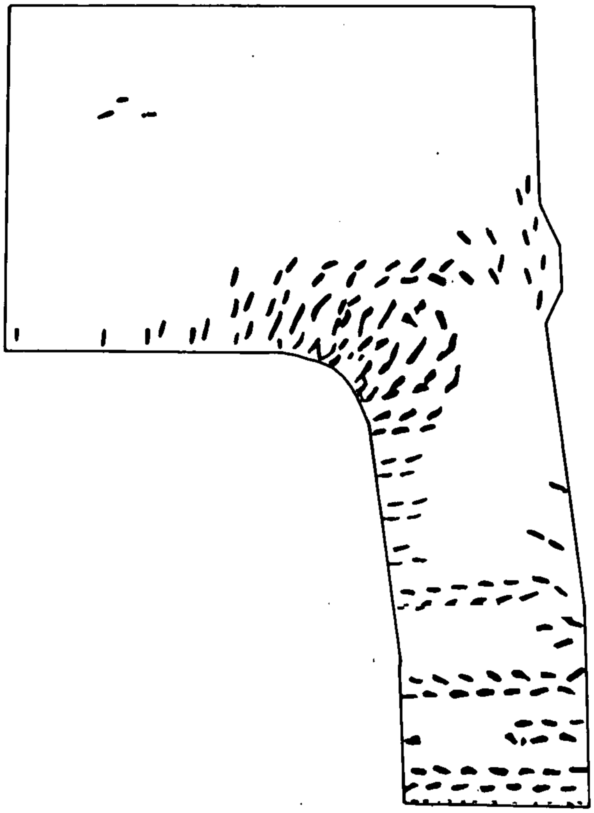

Figure 4-1. Schematic of a typical cracked pattern.

A review of recent developments of fracture mechanics techniques involving bi-axial stress conditions indicates that shear fracture behavior in the liner cannot be overlooked. Recent studies show that the crack propagation rate, the crack orientation, and the critical crack size are dependent on the bi-axial stress ratio. In some instances the ratio of the stresses change the mode of failure from opening mode to shear mode. A typical example of this behavior is depicted in Figure 4-2. For the bi axiality ratio of σ_2/σ_1 = -1 the crack propagates in mode I in the vicinity of the slot, however, once the crack is away from the slot, mode II propagation takes place. For the case where σ_2/σ_1 is less than -1, mode I crack propagation is maintained until the crack penetrates through the thickness. For the liner this type of behavior can be critical even under slight overpressure condition, especially in the areas where the vessel liner intersects the penetration liner. Work on this task has been initiated. When completed, the techniques will be incorporated into the new extended numerical techniques allowing for in-depth analysis of all types of accident conditions.

Core Seismic Response

Based on the computer program discussed in the previous Progress Report, a parametric study of the horizontal mass model shown in Figure 4-3 was carred out. The purpose of the parametric evaluation was to determine:

(a) Validity of a reduced mass model in order to describe a realistic dynamic model.

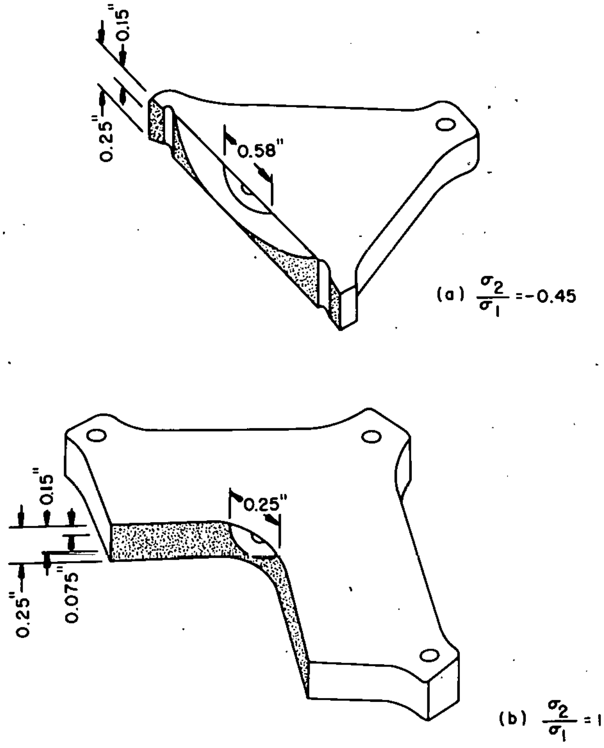

Figure 4-2. Crack failure modes.

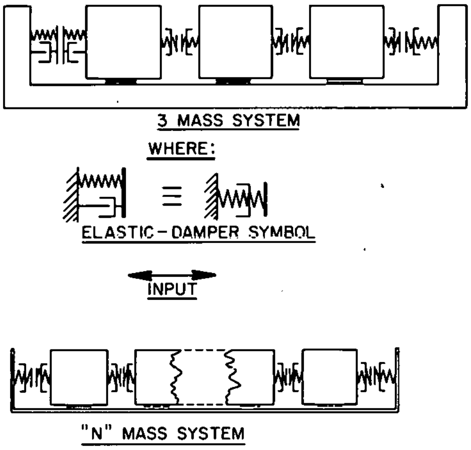

Figure 4-3. Horizontal model.

(b) Sensitivity of response to interelemental and ground damping.

(c) Effect of clearance.

(d) System response to variations in sinusoidal frequency and amplitude.

Figures 4-4 through 4-8 are reproductions of portions of the displacement time computer outputs which are tabulated in Table 4-1. The table summarizes variables of interest for the parametric study for the horizontal model. The top row lists the parameters under investigation. The first item considered was the number of masses for which models were chosen consisting of 5, 7, 9 and 30 masses. In order to study this effect the total mass was held constant with two masses representing the side reflector blocks and the remaining internal fuel elements grouped into packages making up the total mass in the horizontal model. In Run I all of the other parameters were held constant while the number of masses was varied.

The second item considered was that of interelemental damping for which approximate values of 1%, 10%, 30%, and 50% of critical damping were investigated. The model utilized an equivalent set of viscous dampers to simulate the energy dissipated during interelemental collisions. The constant value of critical damping used in Runs I, III, IV, V, was chosen on the basis of the correlation between coefficient of restitution and viscous damping coefficient for equivalent energy dissipation during a collision. Table 4-2 lists the coefficient of restitution determined from the computer outputs for varying interelemental damping coefficients expressed as

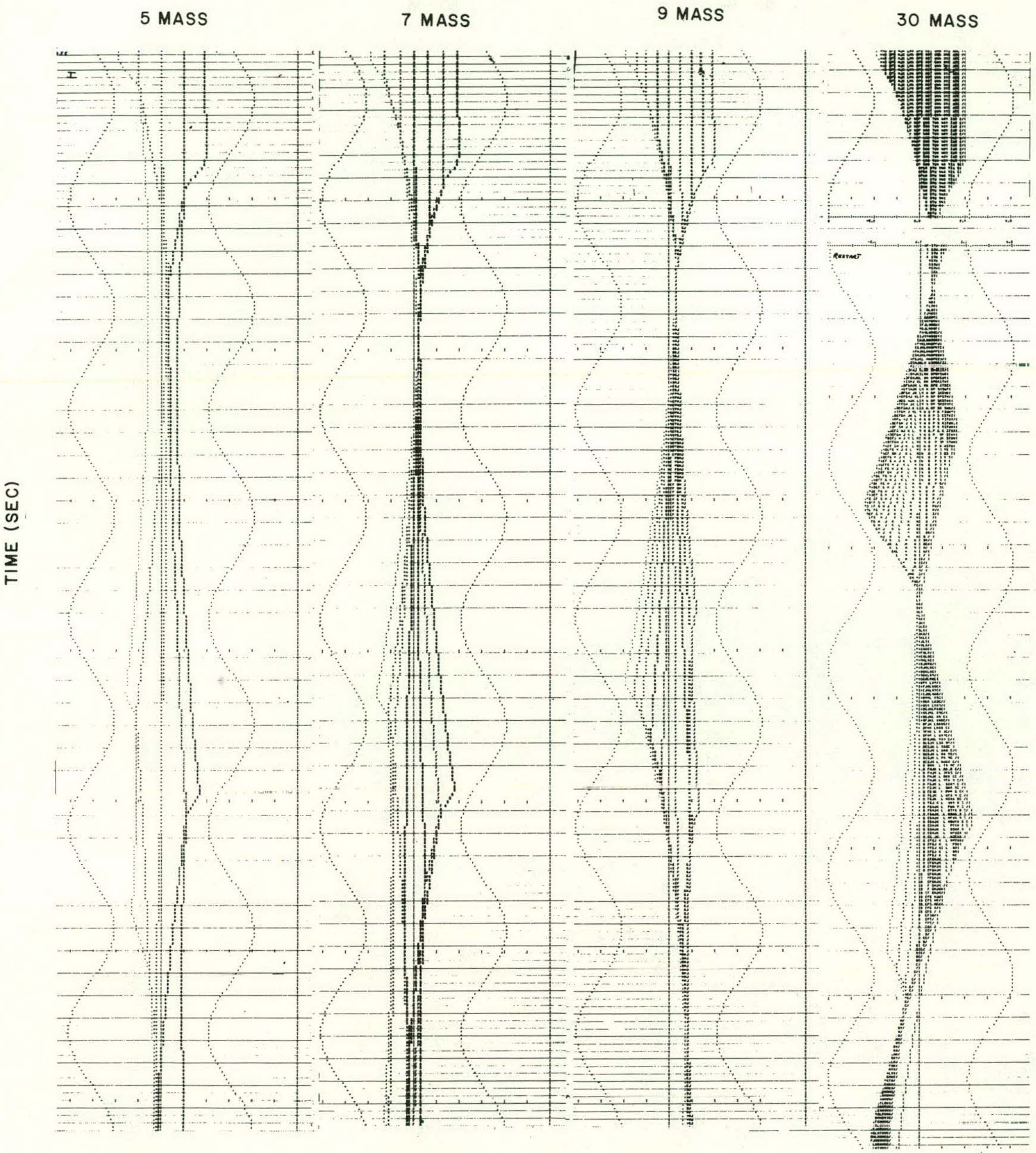

Figure 4-4. Dynamic response of different mass models at $11.4\ \frac{\text{rad.}}{\text{sec.}}$.

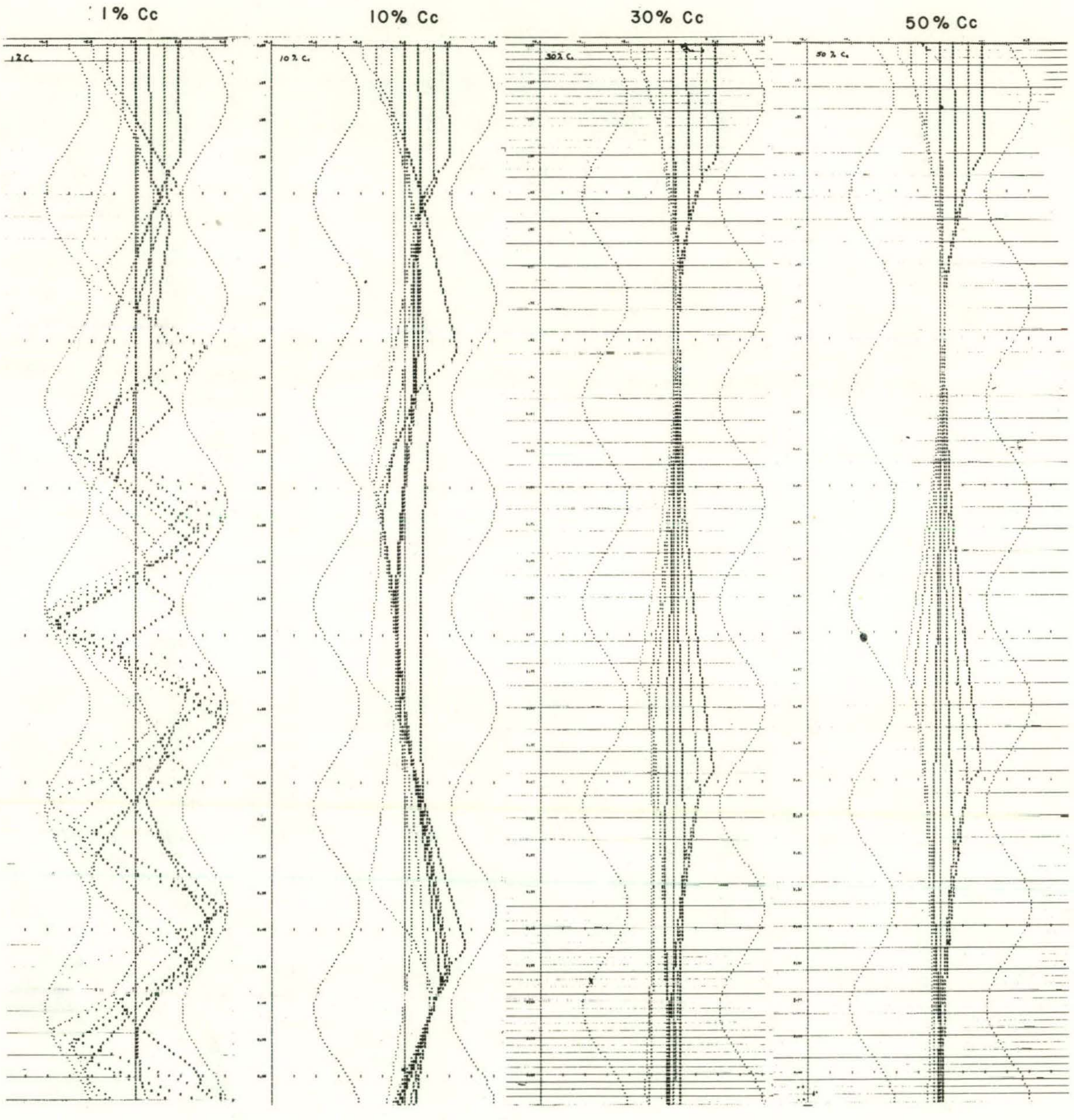

Figure 4-5. Effect of damping on dynamic response of 7 mass model.

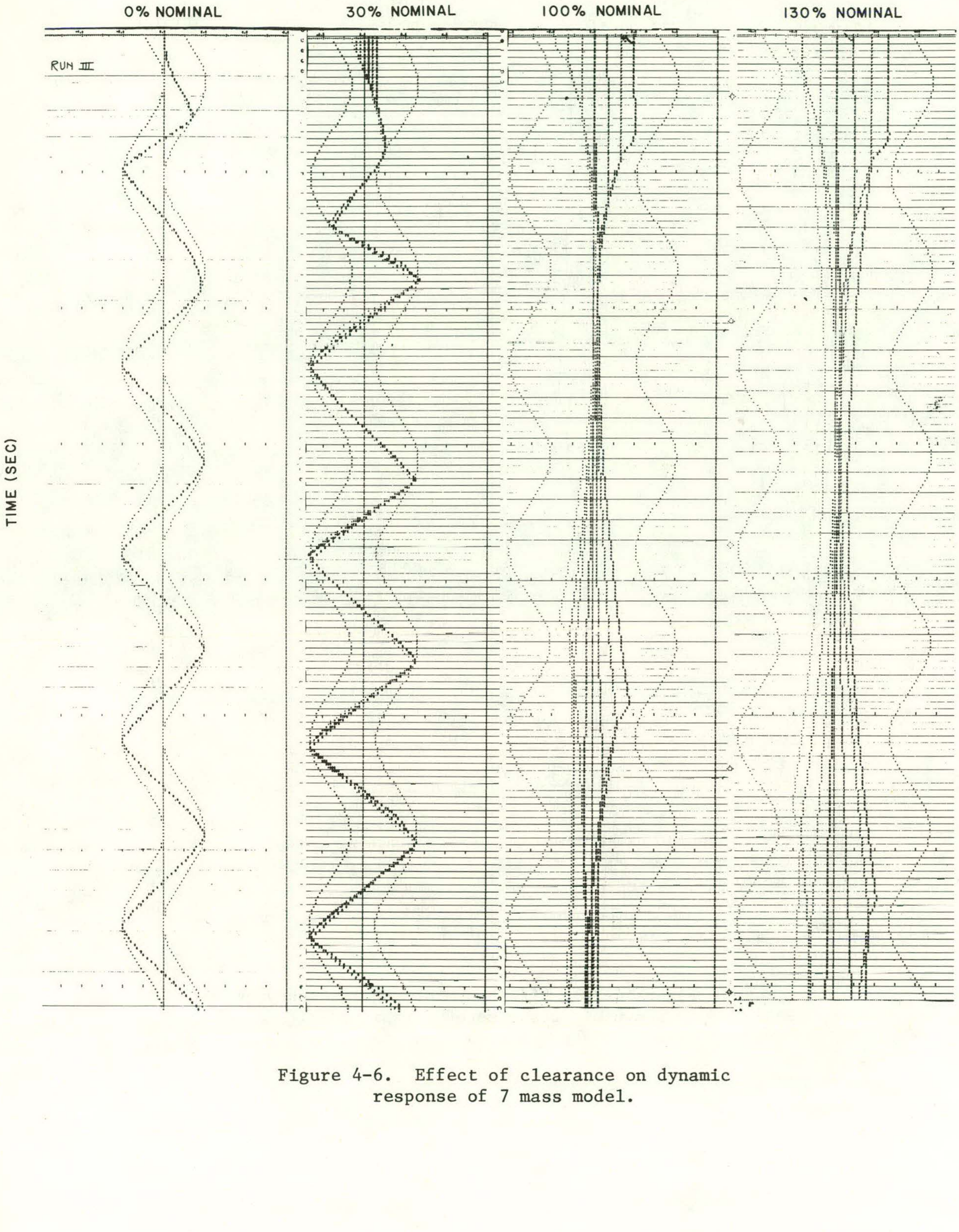

Figure 4-6. Effect of clearance on dynamic response of 7 mass model.

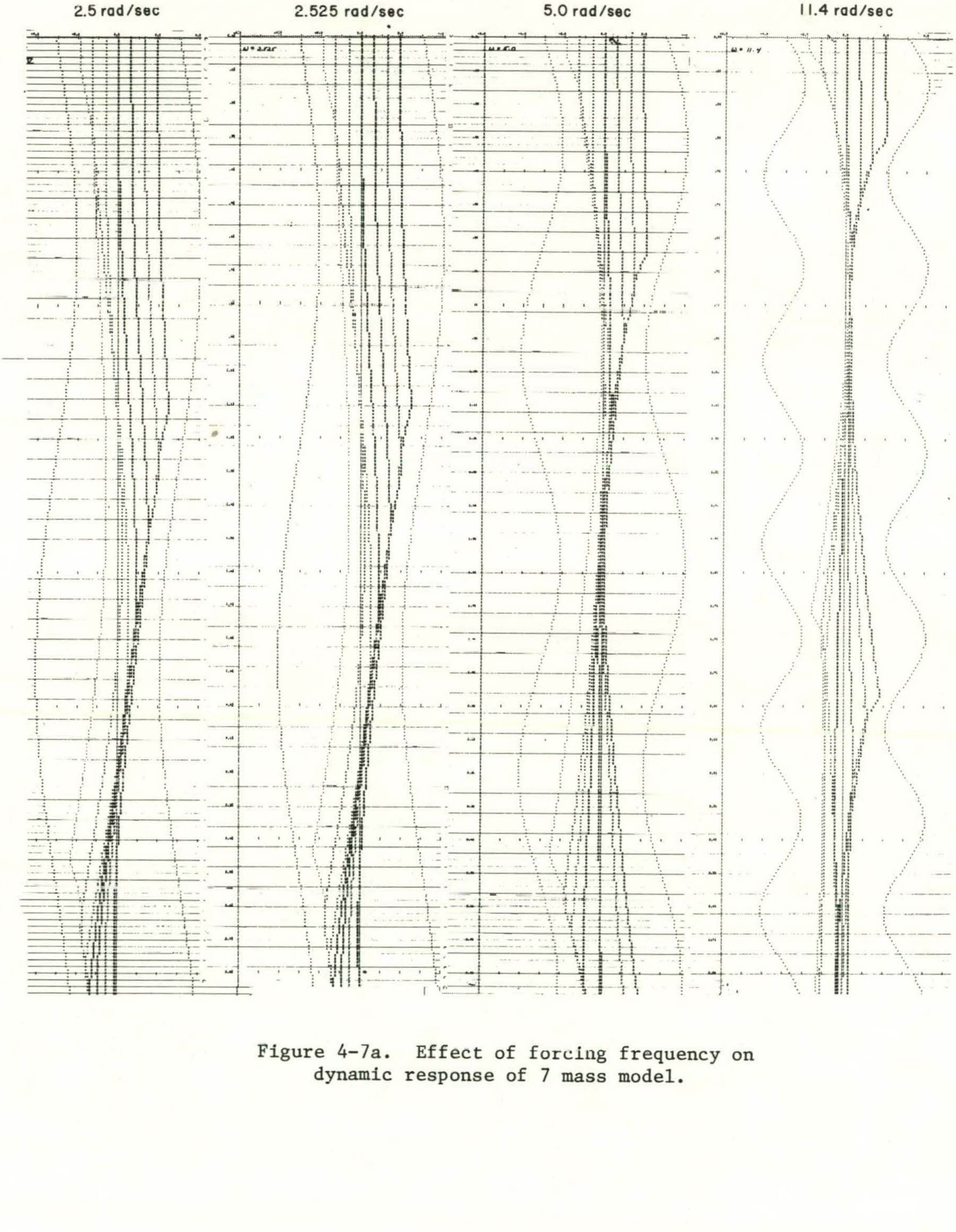

Figure 4-7a. Effect of forcing frequency on dynamic response of 7 mass model.

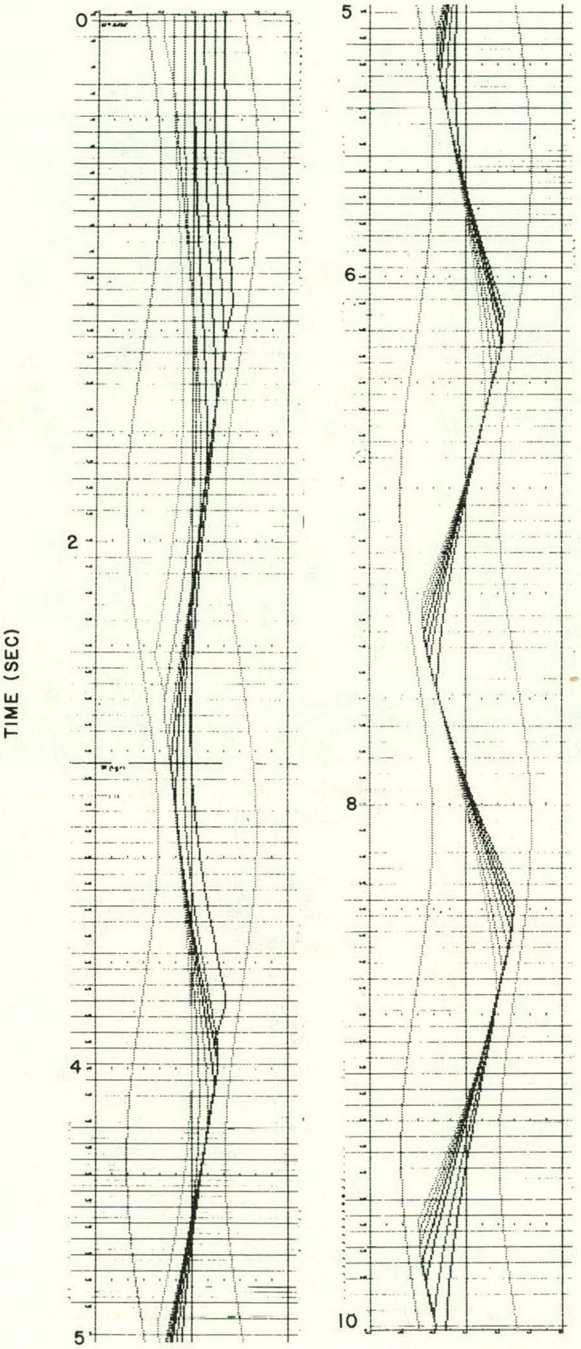

Figure 4-7b. Resonant response of 7 mass model for equal initial spacing of masses.

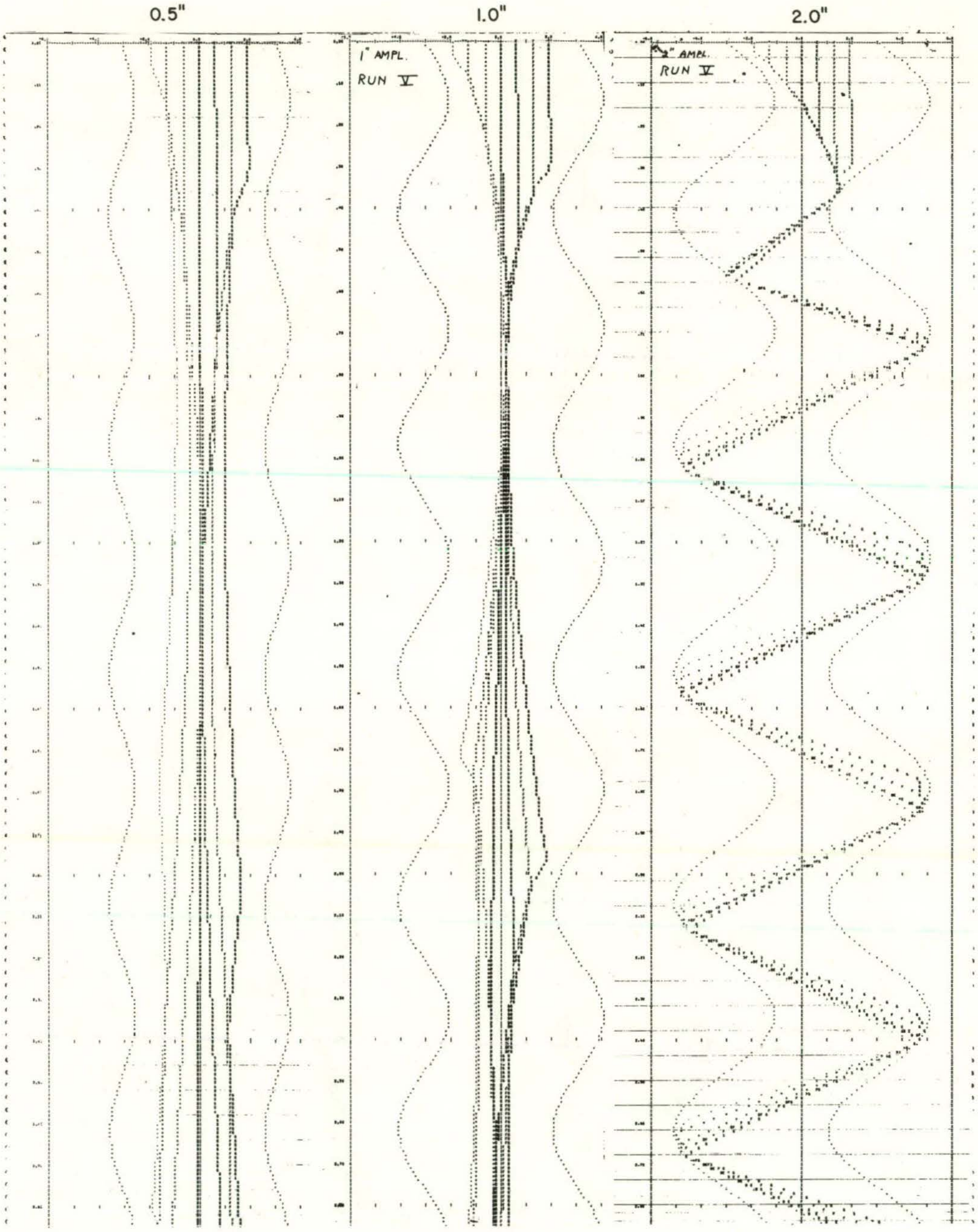

Figure 4-8. Effect of forcing amplitude on dynamic response of 7 mass model.

TABLE 4-1

Parametric Study for Horizontal Model

	Parameter	M	Damping (% Critical)	Clearance (% Nominal)	$\omega\left(\frac{Rad}{Sec}\right)$	Xo (Inches)
I	Number of Masses	5,7,9,30	30%	100%	11.4	1
II	Interelemental Damping	7	1%, 10%, 30%, 50%	100%	11.4	1
III	Total Clearance	7	30%	0, 30%, 100% 130%	11.4	1
IV	Input Frequency	7	30%	100%	2.5, 2.525 5, 11.4	1
V	Input Amplitude	7	30%	100%	11.4	.5,1,2

TABLE 4-2

Evaluation of Coefficient of Restitution

From Viscously Damped Model

(M = 7, Nominal Clearance, ω = 11.4, Xo = 1)

Interelemental Damping (% Critical)	Damping Coefficient $\left(\frac{\text{lb-sec}}{\text{inch}}\right)$	Coefficient of Restitution (Evaluated from Output)
1%	626	.96
10%	6,260	.64
30%	18,800	.23
50%	31,300	.044
100%	62,600	<.001

a % of critical damping for the seven mass model. The value of 30% critical damping was then selected as an approximation to represent the range of values of coefficient of restitution from .15 to .35 (GCR-5:75-4 Oak Ridge National Laboratory February 1975).

The next parameter investigated was that of clearance for which the "N" stands for the nominal diametral clearance of 4.15". In Run III values of clearance were taken from zero to 130% of nominal clearance in order to include the effects of irradiation as well as variation in total clearance depending on the position of the horizontal slice chosen for analysis. For this study the clearances between internal masses was assumed to be equally distributed at t = 0.

The final two columns of Table 4-1 list the frequencies and amplitudes of sinusoidal displacement inputs. A nominal value of 11.4 rad/sec was used as a reference frequency as it represents the natural frequency of the entire mass acting on a single spring pack without clearance. The range of frequencies investigated in Run IV was chosen so as to include the resonant frequency of the system. In Run V amplitudes were varied at a fixed forcing frequency of 11.4 rad/sec which corresponds to input levels of force of about .18 to .7 g's.

Figure 4-9 shows a typical listing of input data and the associated displacement-time output plot for the seven mass system under consideration. Listed on top are the amplitude and frequency

```
SINUISOIDAL IN-PHASE FUNCTION PARAMETERS

AMPLITUDE=         1.00
OMEGAC    =        5.00                 ALPHA=          0.00
NUMBER OF MASSES =   7

     1.10.670     2.26.550     3.26.550     4.26.550     5.26.550
     6.26.550     7.10.670

THERE ARE        8 SPRINGS

  I    SPRING TYPE     KI1          KI2      CHANGE FOR     CI       EXP. FOR        GROUND
         NGAP(I)                             DISP GT                 DISP LT          C(I)

  1             2   0.               .20E+05     -.140      92.390      -1.140      17.735
  2             2   0.               .37E+08     -.645   5248.123-10000.000       44.129
  3             2   0.               .37E+08     -.645   6268.493-10000.000       44.129
  4             2   0.               .37E+08     -.645   6268.493-10000.000       44.129
  5             2   0.               .37E+08     -.645   6268.493-10000.000       44.129
  6             2   0.               .37E+08     -.645   6268.493-10000.000       44.129
  7             2   0.               .37E+08     -.645   5248.123-10000.000       17.735
  8             2   0.               .20E+05     -.140      92.390      -1.140       0.000
```

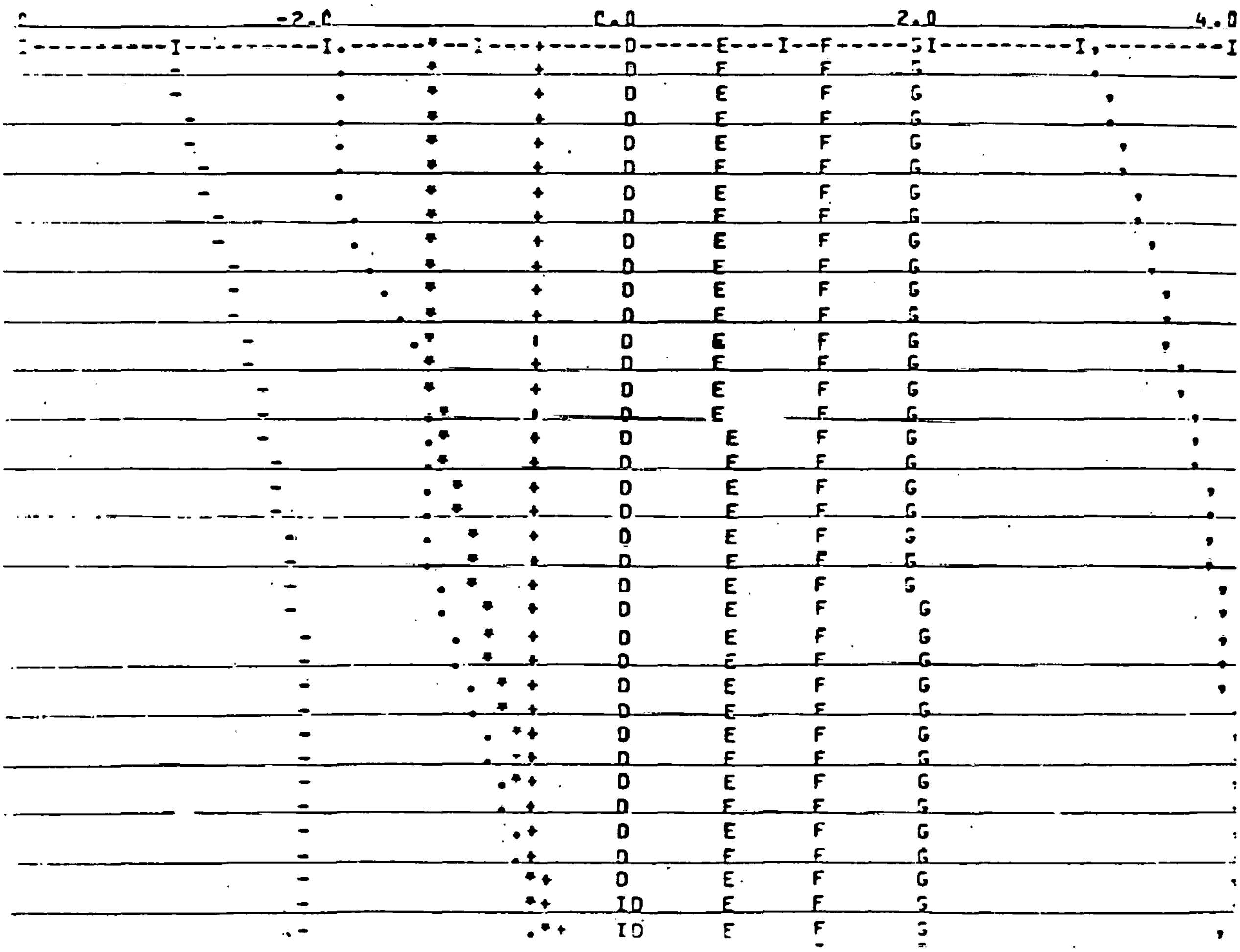

Figure 4-9.

of the sinusoidal displacement input and the number of masses analyzed. The parameter labelled alpha is included so as to permit a linear variation in forcing frequency in order to accommodate studies which necessitate an upward or downward sweep in frequency. In the present case alpha is set equal to zero thereby fixing the input frequency for the entire run. The next set of seven items gives the magnitude of the masses with the first and last values representing the reflector blocks and the five intermediate values representing an equal distribution of internal fuel elements. For each of the eight springs in the model there is tabulated the non-linear spring characteristics, clearance, and equivalent interelemental and ground damping coefficients. The clearances are distributed uniformly depending only on the number of fuel elements included in a grouping of masses with the total clearance equaling the nominal value of 4.15" associated with a horizontal slice of the core. Both the interelemental springs and dampers assume zero value until the clearance between adjacent elements disappears. At this point the springs and dampers take on constant values depending upon the material and geometric properties of the elements as well as the assumed percentage of critical damping. The ground damping coefficient is calculated independently as a function of amplitude, frequency, mass, and coefficient of friction. Both the interelemental and ground damping effects are introduced into the governing differential equations through the mechanism of equivalent viscous dampers.

The plot shown in Figure 4-9 depicts displacement on the horizontal axis and time on the vertical axis. At the top of the plot is shown the initial position of the masses and supporting walls. The points, going from left to right represent the left wall, left reflector block, five internal fuel blocks, right reflector block, and right wall. The spacing between internal points depicts the initial clearances between elements with the spacing between a wall and its adjacent reflector block including the 1" compression of the spring pack in addition to the 0.14" initial clearance.

The symmetrical sinusoidal input of the walls is shown by the outermost two curves and shortly after commencing the motion the left reflector block is imparted motion as the clearance is overcome and compression of the spring pack takes place. As time increases the reflector block is shown to collide with its adjacent fuel block imparting motion to it. A short time later, as shown at the bottom of Figure 4-9, the moving fuel block collides with its adjacent member in a similar manner. Extended displacement-time histories are further shown in Figures 4-4 to 4-8. In addition, the printed numerical outputs for these runs yield the displacements, veclocities, accelerations, and forces for each mass included in the study.

The results of the parametric study for the horizontal model can best be reviewed by referring to Figures 4-4 to 4-8. In Figure 4-4 the starting transients of the displacement-time histories for 5, 7, 9 and 30 mass systems are plotted. For this run the total mass, total clearance, interelemental damping factor, forcing frequency and amplitude are all held constant. In all four cases the initial response is quite similar with collisions taking place from left to right until some degree of clumping occurs. The clumping characteristic is revealed as the mass points approach each other. As the space between elements diminishes the plotting tends towards a single point. Although this characteristic repeats itself, separation of the elements is apparent between these intervals with different response characteristics shown for the several mass models analyzed. Since the complex system of 30 masses requires considerably more computer time than the 5, 7, and 9 mass models, a restart capability has been built into the program and checked out.

Figure 4-5 shows the initial output displacements for interelemental damping ranging from approximately 1% to 50% of critical with mass number, clearance, forcing frequency and amplitude fixed. For the case with 1% of damping the response can best be described as scattered with little indication of clumping. In addition the motion is shown to be quite violent, as indicated by a high state of compression between the reflector blocks and spring packs. As damping is increased to 10% the degree of activity is considerably reduced. This effect continues as damping is increased to 30% and 50% with indications of clumping becoming more apparent. However, a comparison of these last two cases with higher damping shows them to have similar response characteristics.

The effect of varying total clearance with all other parameters held constant is shown in Figure 4-6. For zero clearance the seven masses remain clumped and behave as a single mass responding at close to a resonant condition. As the clearance increases to 30% of nominal only slight departures from clumping are revealed and the system is still in the vicinity of resonance. For both of these cases large forces are developed as the combined mass approaches the walls. When clearance is increased to nominal or 130% of nominal the plot shows a significant change in clumping characteristics and a reduced approach of the internal masses to the walls as well as a lowering in natural frequency of the system to a value considerably below the constant input frequency of 11.4 rad/sec.

In Figure 4-7a displacement-time histories are plotted for several forcing frequencies with all other parameters held constant. Although Figure 4-7a describes only the transient responses for the first 2.5 seconds, further investigation revealed that the natural frequency for the given parameters was approached as $\omega \rightarrow 2.525$ rad/sec. The resonant frequency characteristic is demonstrated more clearly in Figure 4-7b where the plot is carried out for 10 seconds and the steady state resonant response is revealed. Whereas $\omega = 2.5$ rad/sec is in the vicinity of resonance a forcing frequency of 5 rad/sec is shown to produce a subharmonic response as might be expected. This characteristic was suggested after an examination was made of the response record that was obtained at frequency of 11.4 rad/sec which is also shown on Figure 4-7a.

Figure 4-8 presents the outputs for variations in forcing amplitude from 0.5" to 2.0" with all other parameters held constant. At the constant forcing frequency of 11.4 rad/sec this represents an acceleration input approximately in the range of .2 g's to .7 g's. As the amplitude is increased to 2.0" a resonant condition is approached as shown in Figure 4-8. Associated with this condition the masses move together in a regular pattern and clump after striking the boundary.

The sizable forces developed under this condition are indicated in the figure.

Figure 4-10 is a pictorial representation of the dynamic response which includes the effects of forcing frequency and amplitude shown in Figures 4-7 and 4-8. Curve A shows nonlinear resonance occurring at 2.5 rad/sec and a subharmonic response at 5 rad/sec. This is for an input amplitude of 1 inch. Curve B shows the resonant frequency has been increased to 11.4 rad/sec for an input amplitude of 2 inches. The vertical dashed lines represent the stable steady state solutions that would be obtained if the forcing frequencies were swept either up or down.

Simultaneously with the work done on the horizontal array shown in Figure 4-3, the investigation has also progressed on the vertical model shown in Figure 4-11. As the first step towards predicting the response of a single vertical stack of fuel elements a code was developed to analyze the response of a single block subjected to vertical and horizontal ground motions. The block was modeled as a lumped mass with three planar degrees of freedom; horizontal motion, vertical motion and rotation about its center of gravity. The mass is supported on a base of nine spring-dashpot units spaced to simulate a continuous base. It is separated from the side walls by two spring-dashpot units with clearance gaps located at the block upper corners simulating block corner stiffness on side impact. Additionally, two horizontally acting spring-dashpot units with clearance gaps are located on the base to simulate fuel element dowels. A simple

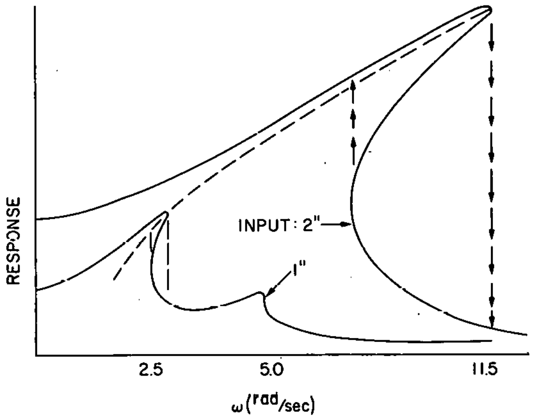

Figure 4-10. Nonlinear response, different input amplitudes subharmonic response at 5 (rad/sec).

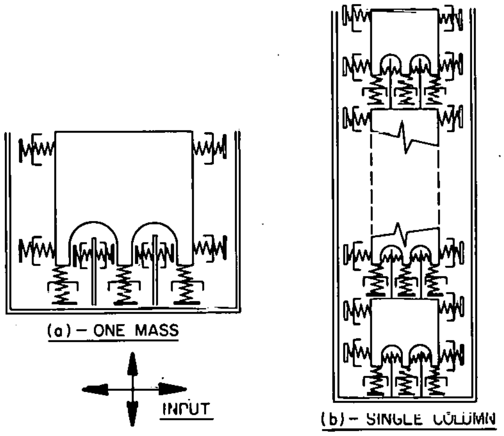

(a) - ONE MASS

(b) - SINGLE COLUMN

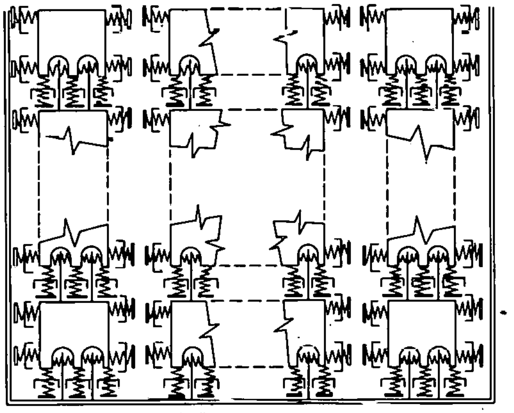

(c) - "N" COLUMNS

Figure 4-11. 3° of freedom for each mass, horizontal & vertical input, one plane.

Coulomb friction effect between block and base is included. A representation of the analytical model is shown in Figure 4-11a.

Figures 4-12 and 4-13 show the computer plotted results for two free vibration analyses for the block. In both figures, although u, w and θ are all shown, the plotting scale factor was selected to depict θ and consequently u and w are for the most part off scale. Both problems show the rocking response which ensues when the block is released after having been initially raised on one corner. In both cases, the time duration of successive periods is reduced as the angle θ becomes smaller. This is a known characteristic of the system. For the problem shown in Figure 4-12, the key parameters were: base stiffness 6,000,000 lb/inch, base damping coefficient 900 lb_f-sec/inch, coefficient of sliding friction 0.2. For the problem shown in Figure 4-13, the parameters were: base stiffness 6,000,000 lb/inch, base damping coefficient 9000 lb_f-sec/inch coefficient of sliding friction 0.0.

Currently, the parametric studies with the horizontal model are being expanded to include the effects of multiple sinusoidal as well as seismic time-history inputs. Simple shake table tests with graphite elements will be undertaken to verify the code results and to investigate and evaluate specific parameters of interest. A user's manual for the horizontal array code, currently under preparation, will be issued. The one block vertical code will be extended to permit the analysis of a single column or stack of elements subjected to

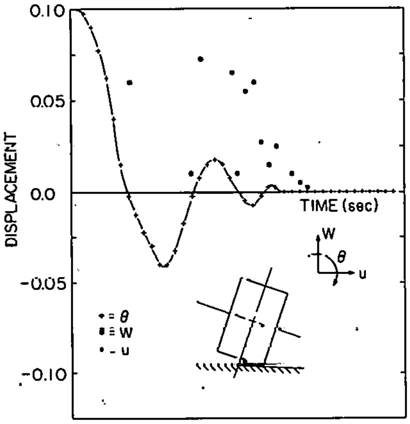

Figure 4-12.

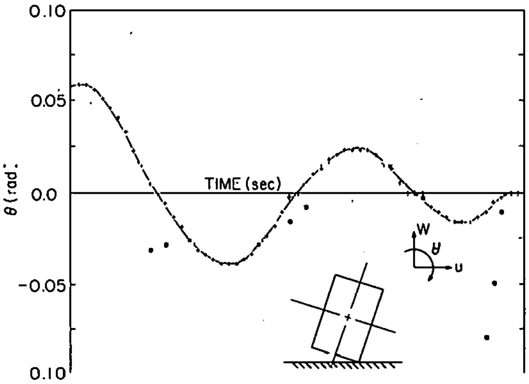

Figure 4-13.

both horizontal and vertical ground motion inputs.

Figures 4-3 and 4-11a depict the limits for which the present analysis techniques apply. Extension of the vertical array code to a single column, Figure 4-11b, is currently under way. With that completed, the horizontal and vertical array codes will be combined to permit an analysis of the multi-column system depicted in Figure 4-11c which in essence is a two-dimensional array of elements. As a long range goal we envision the further extension of the composite code to include the effects of posts, Figure 4-14, three-dimensional hexagonal block arrays, Figure 4-16.

Core and Core Support Structures

Progress has been made in the area of core and core support structures. The study includes review of HTGR graphite properties, development of failure criteria and modification of finite element programs for fuel element analysis.

Material properties of H-327 and H-451 graphites in terms of elastic moduli, thermal expansivity, tensile and compressive strength, thermal conductivity, dimensional changes, creep and oxidation rate are being gathered and studied. The purpose of this review work is to identify the material data that are not presently available, but are needed for safety analysis.

As reported in the previous Progress Report, a failure criterion for predicting the fracture strength of graphite under a

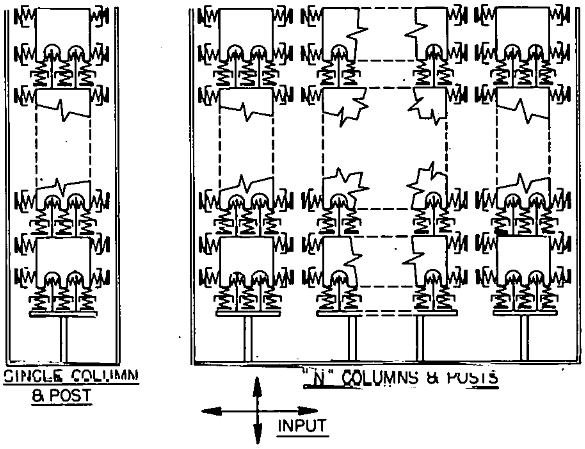

Figure 4-14. 3° of freedom for each mass, horizontal & vertical input, one plane.

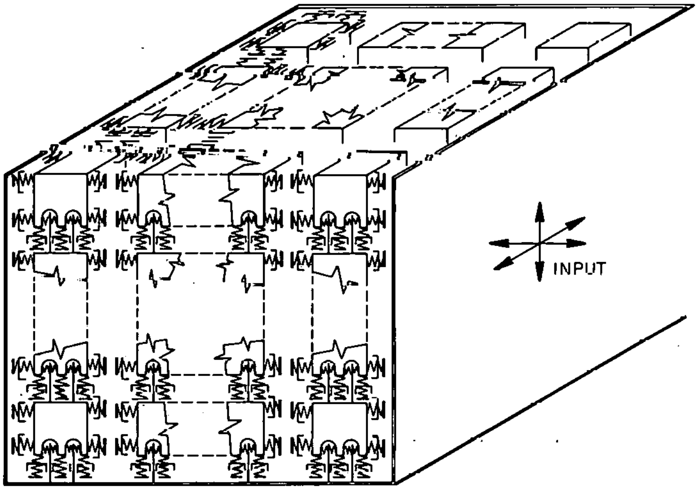

Figure 4-15. 6 degrees of freedom for each mass, 3-D input.

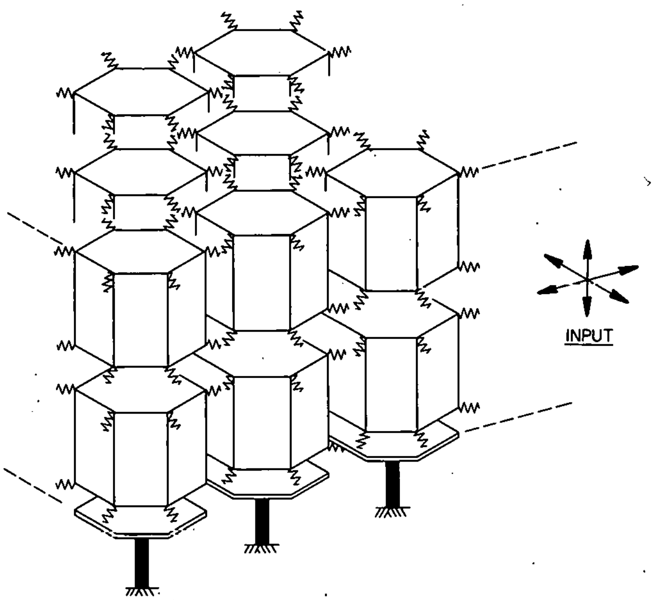

Figure 4-16. Hexagonal element 3-D input.

multi-axial stress state was proposed. Further evaluation of the theory by test data indicated that the proposed theory gave fairly good strength prediction for graphites thus far investigated. A computer method by use of least square curve fit has been developed to characterize the theory by the use of experimental data. This program has been tested out for three different grades and the strength coefficients were conveniently obtained by the computer analysis.

Work is underway to modify an existing BNL elastic-plastic-creep computer program for the structural analysis of HTGR fuel elements and reflector blocks. The modifications involve treatment of transversely-orthotropic material properties, inclusion of creep and dimensional changes due to irradiation. This program will soon be applied to determining the structural response of a typical HTGR fuel element. Further extension of this program will include the failure criterion of graphite for the structural evaluation of HTGR core design.

V. Materials

The work in this program area covers four groups of materials: (1) metals, (2) graphites, (3) PCRV, and (4) other materials, which include control rod and thermal barrier insulation. Objectives are to assess and review the state of the art, to identify the critical areas pertinent to HTGR safety and initiate an experimental program to obtain data pertinent to safety.

The review and assessment of the state of the art is progressing in the areas of metals, graphites and PCRV. Study will be started on control rod and thermal barrier materials during the next report period.

An experimental program has been initiated on the metal components, and on graphites. For the metal components, equipment is being set up to study creep, creep rupture, high cycle fatigue, low cycle fatigue and tensile properties. Studies will be made in air and in normal HTGR environments and under abnormal operating conditions. The mechanical testing program will be supported by metallographic studies to determine the failure mechanisms involved.

Equipment is being set up to study the effect of oxidation on the strength of ATJ graphite core support posts, PGX core support blocks, and H-451 core moderator graphites.

Aerospace Corporation, under contract to BNL, is studying the fracture mechanism of these graphites. This work is summarized below:

A. Metal Components (J. G. Y. Chow)

Our assessment and review indicates that many of the metal components proposed for use in HTGR primary coolant circuits are special alloys which have had only limited service experience. It is evident that there is insufficient information available on long term effects on all the highly alloyed materials such as Incoloy 800, Hastelloy X, Inconel 750, Inconel 718, and Inconel 617. Furthermore, in most cases elevated temperature design data necessary for inelastic and creep fatigue interaction analysis are not available. This design data is important because failure of some of these metal components could have safety implications.

A supply of these alloys and other alloys such as 2¼Cr-1Mo and some of the martensitic stainless steels are being purchased for study in our mechanical and corrosion testing program.

Fatigue Testing of Incoloy 800

Incoloy 800 (45 Fe, 20 Cr, 32 Ni) is an austentic steel that is used in several important components in the primary system of the HTGR. Incoloy 800 has high temperature mechanical properties superior to the 300 series stainless steels (above 1100°F) and is also more resistant to stress corrosion. However, Incoloy 800 is a relatively new alloy and its long term experience is not nearly as extensive as the more common austentic stainless steels.

A program on the high cycle and low cycle fatigure testing of Incoloy 800 has been started. Initially, the testing will be done in air at temperatures up to 1400°F. Equipment is being constructed to pre-expose test specimens in impure helium environments that might be encountered in an HTGR. Individual testing units will be equipped with chambers to perform the fatigue test in HTGR helium environments. We are planning to use a capsule with a bellows as an environmental test chamber for the specimen. Figure 5-1 shows such a capsule being set up in a MTS system electrohydraulic testing frame.

At the present, we only have capability to perform load controlled high cycle fatigue tests. Low cycle fatigue testing equipment, where the diametric strain controls the fatigue cycle, is being purchased.

Figure 5-2 presents the load controlled high cycle fatigue (S-N) alternating stress vs. cycles to failure curve of Incoloy 800 at 1100, 1200, and 1400°F. These tests were performed in MTS push-pull units at 40 cps. The material tested is from the Hanford controlled lots that were purchased for the AEC irradiation effects program. The material was solution annealed at 2100°F prior to testing.

The data presented show that Incoloy 800 exhibits endurance limits at 1100 and 1200°F but at 1400°F, the S-N curve continues to slope downward at cycles to failure of 1×10^8. Additional tests are being run to ascertain the mechanical behavior at about 12,000 psi alternate stress level. Examination of the 1400°F fractured specimens indicates that the fatigue crack was initiated at the surface. Metallographic examination will be performed to determine whether preferential grain boundary oxidation or internal microstructural instability at 1400°F is causing the slope in the S-N curve.

Mean load tests on Incoloy 800 have been performed at 1100°F and at 1200°F. Figure 5-3 presents mean load test data at 1100°F at mean loads of 10,000 and 20,000 psi plotted on the Goodman diagram. At 1100°F, the Goodman approximation of the mean load

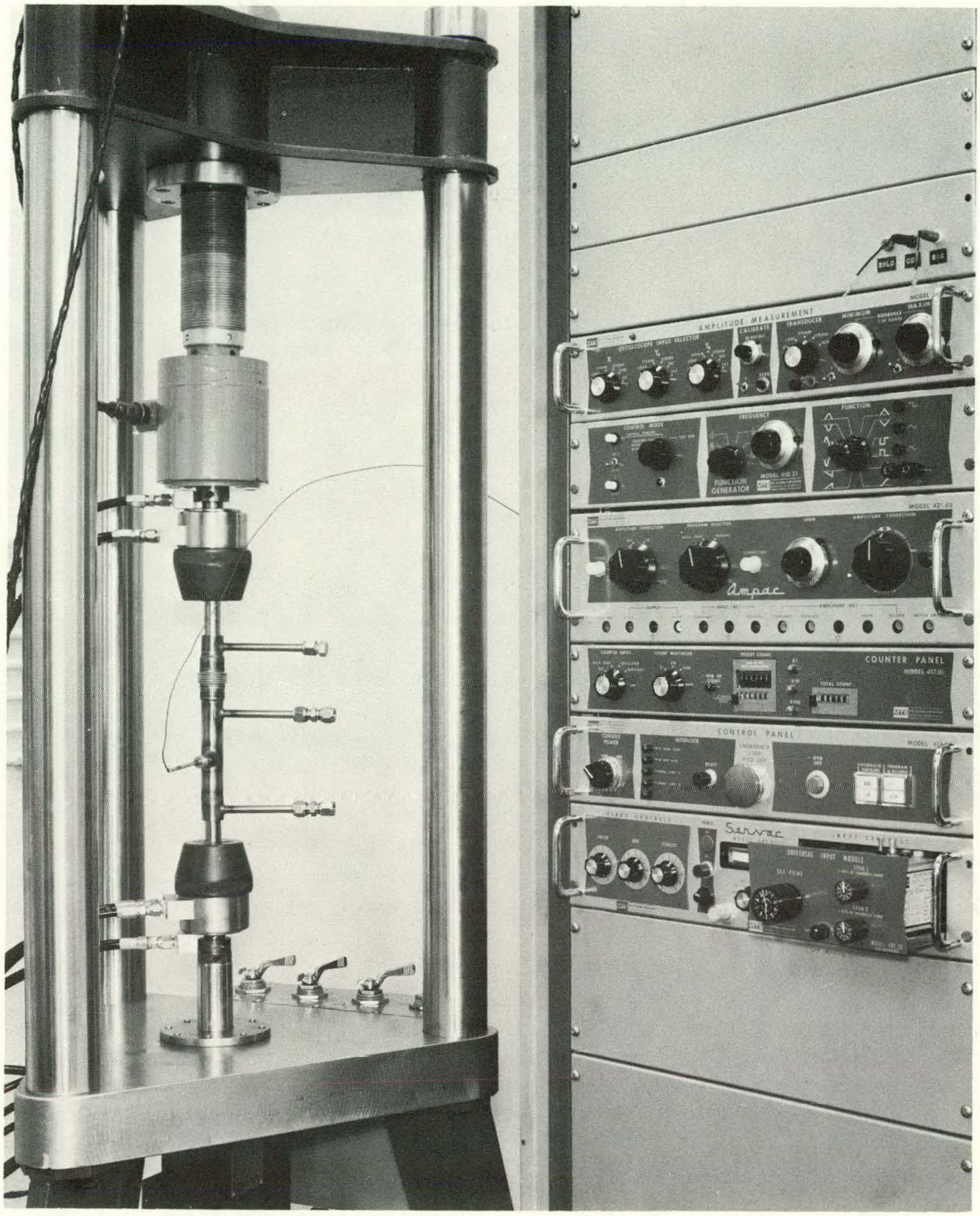
AMPLITUDE MEASUREMENT
OSCILLOSCOPE INPUT SELECTOR
CALIBRATE
TRANSDUCER
MINIMUM
FREQUENCY
FUNCTION
CONTROL MODE
FUNCTION GENERATOR
Ampac
COUNTER PANEL
CONTROL PANEL
EMERGENCY STOP
Servac
UNIVERSAL INPUT MODULE

Figure 5-1.

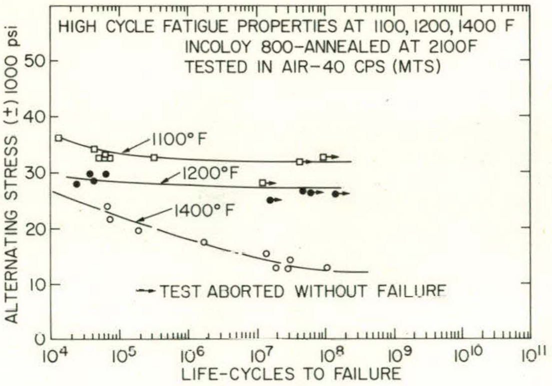

Figure 5-2. High cycle fatigue properties at 1100, 1200, 1400 F, incology 800 - annealed at 2100 F, tested in air - 40 CPS (MTS).

effects appears to be quite accurate.

Figure 5-4 presents mean load test data (1200°F) at mean loads of 10,000 and 15,000 psi plotted on the Goodman diagram. At 1200°F, the data are below the maximum stress line and the Goodman approximateion may not be an accurate representation. Further testing is required to determine the effect of mean load on the high cycle fatigue behavior of Incoloy 800.

Creep Rupture Testing of Incoloy 800

Four creep rupture units are being set up for testing at 1100°F to 1400°F. Initially the tests will be performed in air. Once the basic behavior in air has been determined, tests will be performed in impure helium using a bellows capsule to contain the environment similar to that shown in Figure 5-1.

B. Graphite Components (J. G. Y. Chow)

Equipment is being set up to determine the tensile properties of ATJ, PGX, and H-451 graphite before and after exposure to He environments. Testing will be performed following the ASTM procedure. This procedure consists of cementing right cylindrical specimens to metal end pieces with epoxy. The load is applied through roller link chains to maintain uniaxial alignment during pulling.

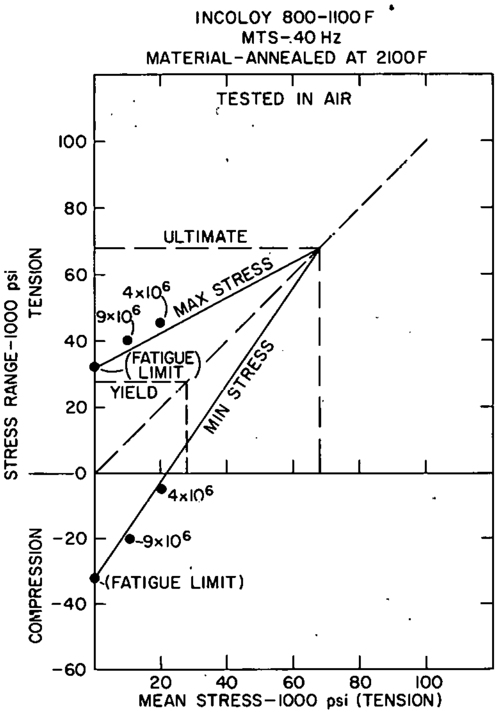

Figure 5-3. Goodman diagram.

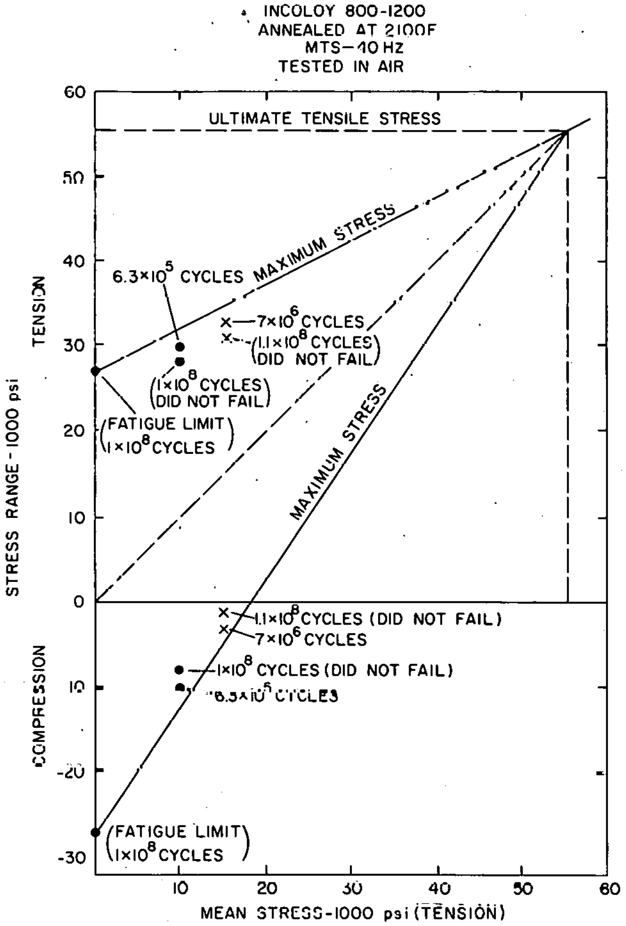

Figure 5-4. Goodman diagram.

C. Microstructure and Fracture of HTGR Graphites (J. E. Zimmer and R. A. Meyer -- The Aerospace Corporation)

This program is directed towards the study of the relation between microstructure and fracture of graphites used in high temperature, gas cooled nuclear reactors. The aim of this work is to provide information that will aid in precisely defining the behavior of graphitic materials during normal reactor operation and under various reactor environments. This information will be used to provide improved bases for the evaluation of reactor safety.

The approach for this program is to determine the relation of microstructure to the mechanical and fracture behavior of HTGR graphites and the effect of various reactor environments on these relationships. Initially, crack initiation and propagation studies are being conducted on two HTGR graphites: Union Carbide ATJ graphite used for structural support posts and Great Lakes Carbon H-451 moderator graphite. A wedge opening, crack propagation specimen is stressed and observed in the scanning electron microscope. This specimen is 2 mm thick with a half thickness, V shaped groove along the back to assure a relatively straight crack path. Controlled crack growth occurs with this specimen and direct observation of cracking and the graphite microstructure is made. Ion etching with xenon of the specimen surface delineates the individual microstructural features present, which provides identification of the microstructure at each point along the crack path.

The microconstituents that comprise ATJ graphite are filler coke particles, binder, and regions of impregnant. Each of these has a characteristic morphology that is brought out by the ion etching. An example is shown in Figure 5-5. The regions with the series of parallel lines are needle coke grains sectioned parallel to the needle axis. The regions of binder around these grains are not as easily identifiable due to the complexity of their morphology. A typical section of the crack path is shown in Figure 5-6. The crack tends to follow the microstructure, producing the jagged appearance. Generally, cracking occurs by cleavage parallel to the graphitic basal layers. This is evident in Figure 5-7 where the crack is parallel to the etching striations representing the graphitic layers. However, when a needle coke grain is oriented with its set of parallel layers perpendicular to the advancing crack, the crack tends to go around the grain, as shown in Figures 5-7 and 5-8. Thus, the crack path in ATJ graphite is dependent in part on the easy cleavage direction of graphitic grains and on the relative orientation of the acicular grains to the crack direction. Changes in the direction and mode of crack propagation occur on a scale equivalent to the 70-micron, average grain size in ATJ graphite.

The H-451 moderator graphite is a coarser grain graphite with the individual grains having an isotropic morphology. The crack path (Figure 5-9) appears similar to that for the ATJ graphite, except that the microstructural features are much larger and local deviations in the crack direction occur on this larger (about 600 microns) scale. In regions where the structure is needle like, the crack tends to follow

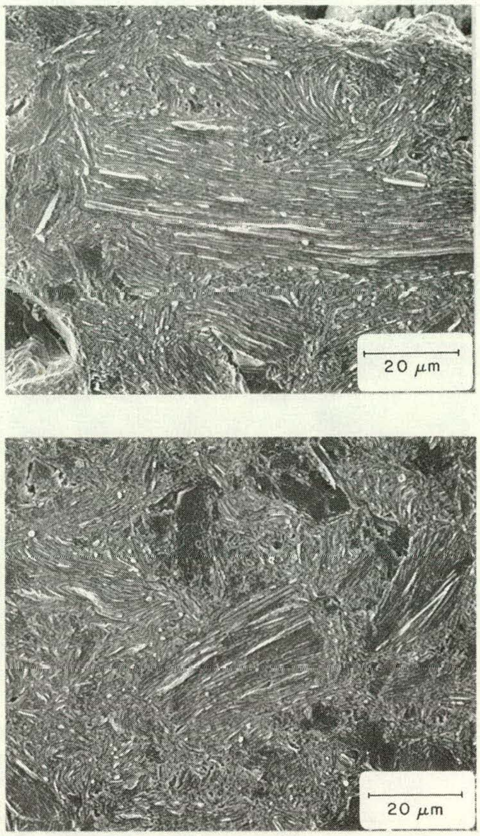

Figure 5-5. Scanning electron micrographs of the longitudinal section of needle coke grains in ATJ graphite, xenon ion etched.

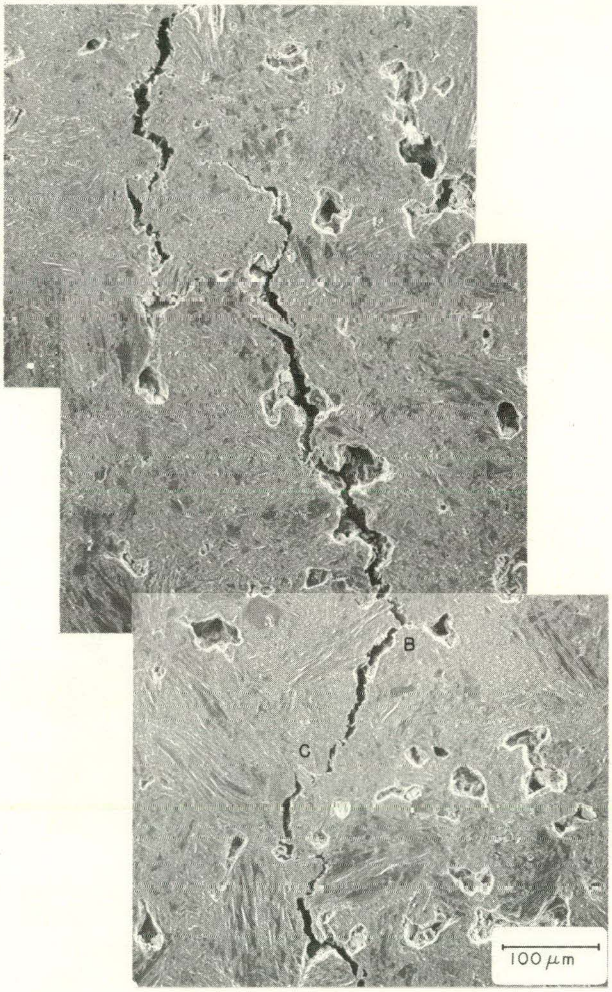

Figure 5-6. Scanning electron micrograph of crack path in ATJ graphite, xenon ion etched.

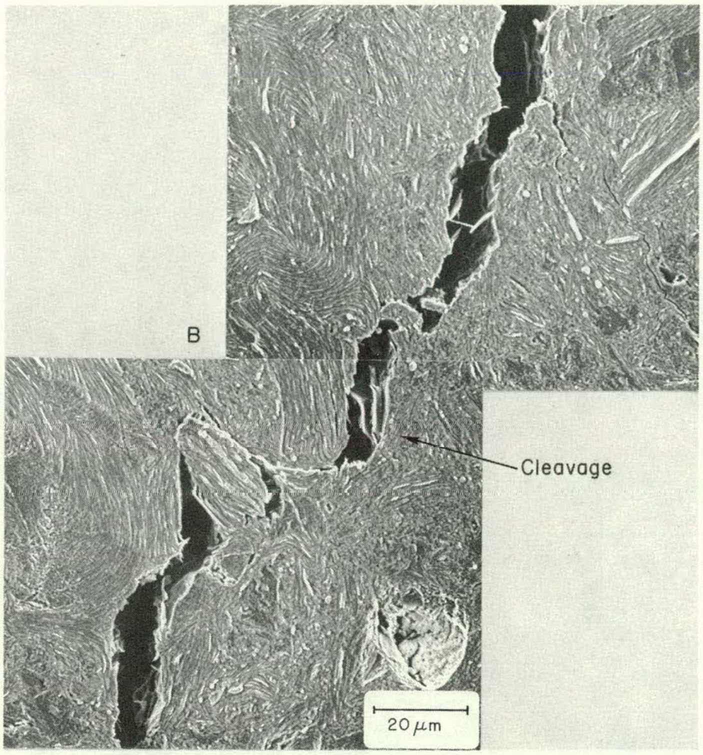

Figure 5-7. Scanning electron micrograph of crack path in ATJ graphite showing effect of grain orientation.

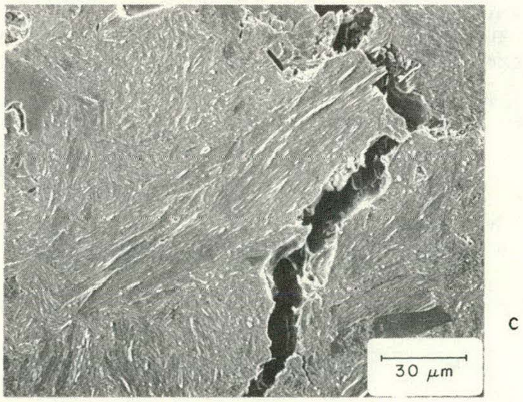

Figure 5-8. Scanning electron micrograph of crack path around unfavorably oriented needle coke grain in ATJ graphite.

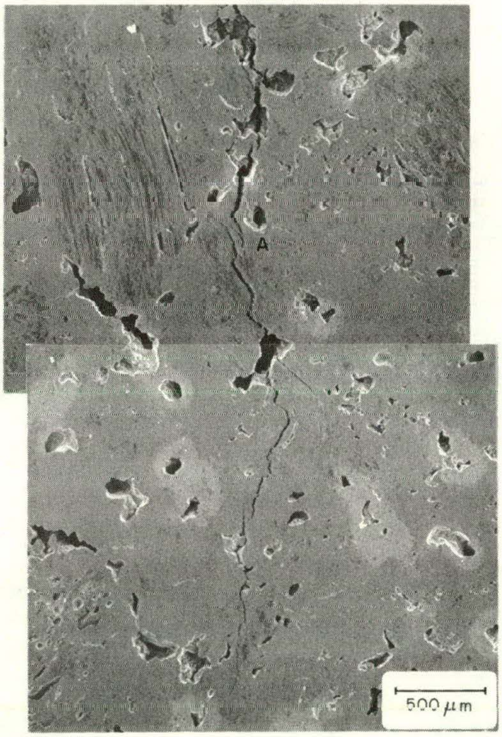

Figure 5-9. Scanning electron micrograph of crack path in H451 graphite, xenon ion etched.

the parallel graphitic layers, as shown in Figure 5-10. The cleavage strength is fairly low, leading to multiple fracturing. Exfoliation of the graphitic layers is also evident.

The major microconstituents of this graphite, filler grains and binder, have a fine isotropic structure. This structure consists of tightly folded graphitic layers randomly oriented in all directions. The fine isotropic structure, after sectioning and etching, is shown in Figure 5-11. The darker, featureless areas are regions where the graphitic layers are parallel to the specimen surface. Where the basal layers are perpendicular to the specimen surface, the etched structure appears as parallel light lines separated by dark lines. These dark lines are small cracks between crystallites that developed upon cool down from graphitization. A crack traversing this fine isotropic structure has a jagged appearance (Figure 5-12) corresponding to its tightly folded pattern of graphitic layers. Thus, initial observations suggest that the crack path in H-451 graphite is dependent on the fine isotropic structure within the filler grains and on the large amount of porosity present (Figure 5-9).

The crack propagation studies on ATJ and H-451 graphite will continue. Similar studies will be initiated on PGX graphite used for the HTGR support blocks. Studies of the effect of oxidation on the microstructure and fracture behavior of these graphites will also be initiated. The initial observations of crack propagation in the ATJ and H-451 graphites indicate that primary modes of fracturing are different in these two graphites. The changes in microstructure as a result of oxidation are expected to also be different for these two

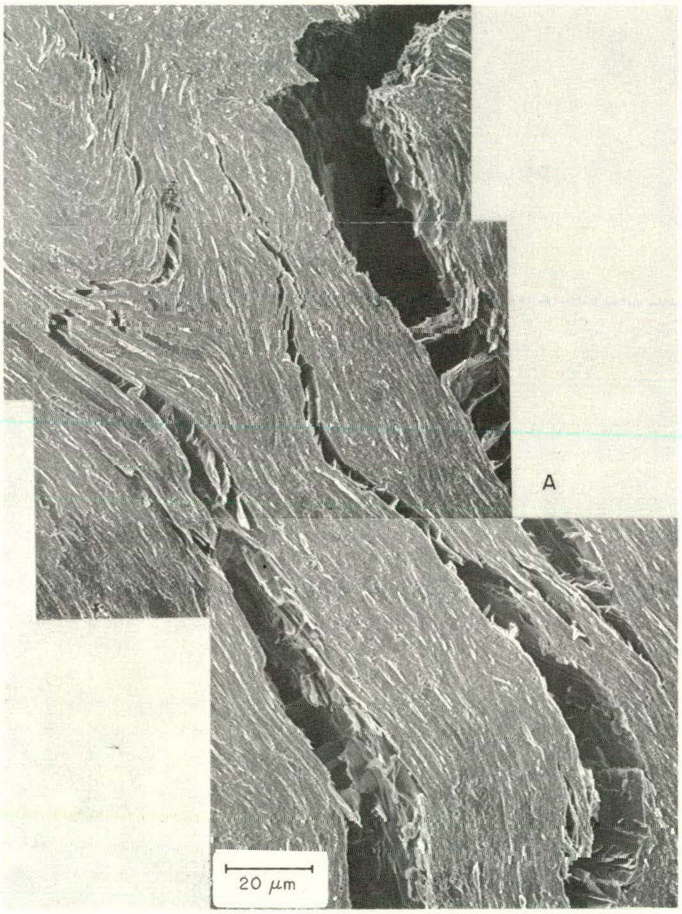

Figure 5-10. Scanning electron micrograph of crack path in needle-like region of H451 graphite.

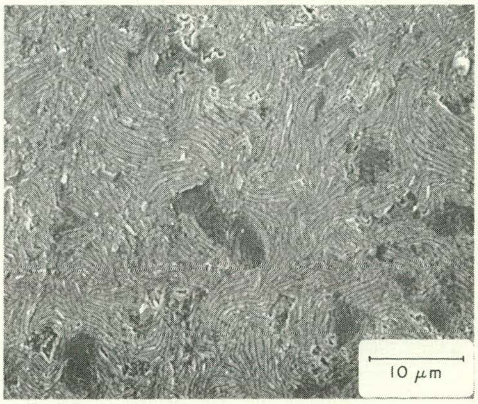

Figure 5-11. Scanning electron micrograph of fine isotropic structure of H451 graphite.

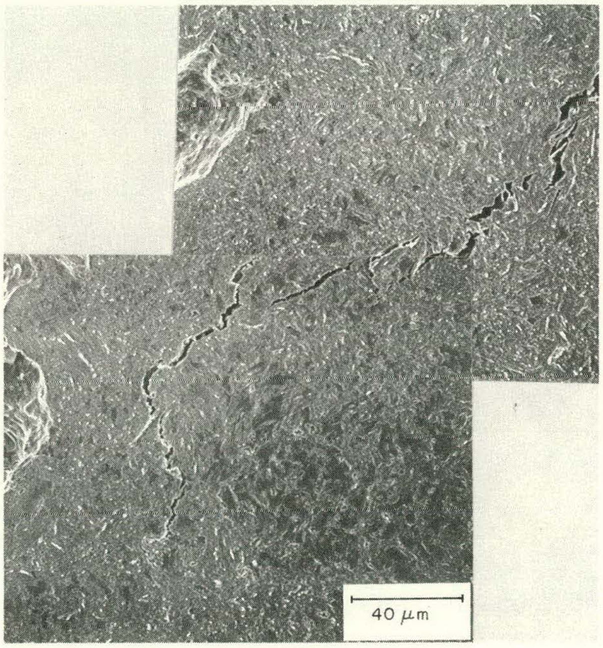

Figure 5-12. Scanning electron micrograph of crack path in fine isotropic structure of H451 graphite.

graphites, thus identification of the modes of fracture pre- and post-oxidation should provide valuable information about their structural integrity.

D. Compilation and Assessment of Properties of Concrete for Use in Establishing Criteria for PCRV Safety Analysis

(A. Auskern and L. E. Kukacka)

A review of the literature to determine values for the engineering properties of concrete at the environmental conditions present in PCRV's under normal operating conditions (up to 93°C) is continuing.

In compiling PCRV property data, it is important to realize that the heated portion of the vessel concrete, surrounded on one side by the steel liner and on the other by water-saturated cool concrete, can be assumed to be sealed in terms of the anticipated ease of moisture loss on heating. Thus, depending on the actual temperature level attained, part or all of the free moisture may be retained and the implications of the presence of water as a mineralogical phase in the heated concrete must be considered. It is therefore logical to question whether property data taken at atmospheric pressure in which the free moisture can evaporate and be removed as a phase during heating have any relevance when considering the effects of temperature exposure on concrete in the PCRV environment[5-1].

During the current report period data pertaining to compressive strength, flexural strength, shrinkage, and creep were compiled. The results obtained to date are summarized below. Data for thermal conductivity and diffusivity were given in the previous report.

Shrinkage

Aged concrete subsequently heated in air at atmospheric pressure will undergo dimensional changes as a result of the following processes:

1. Loss of free water (evaporable) from the concrete.
2. Loss of chemically combined (nonevaporable) water from the hydrated cement phases.
3. Thermal expansion of the concrete.

Shrinkage associated with the loss of free water under normal conditions is termed drying shrinkage. The complete removal of evaporable water as a result of heating can result in a shrinkage of over 2% in the volume of the cement paste[5-2]. However, the presence of aggregate limits the shrinkage of concrete to about one-tenth of that possible in cement. The amount of shrinkage is proportional to the amount of water lost.

Heating to a temperature of 260°C will remove the chemically combined water from hydrated cement. The shrinkage that accompanies this loss of water may produce cracking. Carbonation of $Ca(OH)_2$ can also occur on heating the cured cement phase at atmospheric pressure. The extent of carbonation dictates the dimensional changes that this reaction will produce in the heated gel.

On initial heating of saturated concrete both the aggregate and cement phases expand. In practice it is difficult if not impossible to measure the thermal expansion of saturated concrete on heating at atmospheric pressure for several reasons:

1. Moisture is lost continuously over the temperature range of interest (20° to 260°C). Since the expansion coefficient of wet concrete is not the same as that of dry concrete, the problem becomes one of attempting a property measurement under conditions where the property itself is continually changing.

2. Shrinkage effects accompanying moisture losses reduce the overall magnitude of the expansive strains due to thermal expansion.

Values reported in the literature for the thermal expansion coefficient of concrete range from $\sim 3 \times 10^{-6}$ in./in./$^\circ$F to as high as 18×10^{-6} in./in./$^\circ$F. The majority of data fall in the 3×10^{-6} to 6×10^{-6} in./in./$^\circ$F range.

Estimates for the total shrinkage of a 42-in. containment wall sealed on the inner surface with a steel liner and with a sealing compound on the outer surface have been presented by Graham[5-3]. The total predicted shrinkage strain over a 40-year period is $\sim 100 \times 10^{-6}$ in./in. for a 2-in. slump concrete. Increases in slump to 3 and 4 in. result in strains of 150 and 200×10^{-6} in./in., respectively. These values would be expected to increase at higher operating conditions.

Very limited literature data on the shrinkage properties of water-saturated concrete at elevated temperatures are available. One series of tests in which water-saturated concrete was heated to 260°C was performed by Lankard[5-1]. In this work specimens exhibiting a 28-day compressive strength of $\sim$6000 psi were heated in autoclaves to 80°, 121°, 190°, and 260°C. In this manner the saturated steam pressure commensurate with a given test temperature was allowed to develop over the specimens.

Although the primary purpose of Lankard's work was to determine the effect of high temperature on the compressive strength, flexural strength, and modulus of elasticity, one observation about shrinkage was made. Compared to samples heated at atmospheric pressure, the water-saturated specimen exhibited greater dilation due to thermal expansion since no concomitant drying shrinkage was occurring.

Creep

Data on the creep rate of water-saturated concrete at temperatures >100°C have not been found in the literature, probably due to the difficulty in performing the tests.

During the current report period results from tests performed with dry specimens at temperatures up to 427°C and at various moisture contents at 20° and 60°C have been reviewed[5-4,5-5]. The conclusions from these studies are summarized below:

Dry Concrete at Temperatures up to 427°C[5-4]

1. The shape of the creep curves of concrete at elevated temperatures is the same as that at room temperature.

2. The stress/strength ratio has a greater effect on creep than elevated temperature.

3. A non-linear relationship between creep and the stress/strength ratio exists.

Effects of Moisture on the Creep of Concrete at Temperatures up to 60°C

1. The creep increases linearly with the moisture content.

2. The ratio of creep at an elevated temperature to the creep at normal temperature is approximately constant irrespective of time and the moisture content.

3. The decrease in creep at temperatures near 100°C reported by many workers is probably caused by drying prior to loading.

4. In massive construction where the concrete must be assumed to be water-saturated, a considerably increased rate of creep above 100°C compared with that of dried specimens should be expected.

Compressive Strength

In previous discussions of the mechanical properties of concrete for HTGR pressure vessel application, concrete specifications for different HTGR's were compared (BNL 19763) and some of the factors that can affect the compressive strength in the PCRV environment were discussed (BNL 50450). In this report the PCRV environmental factors and their effect on concrete strength will be discussed in more detail. Areas where data are lacking will be pointed out.

It was mentioned in the previous progress report that the strength of a given PCRV concrete is intimately related to its temperature-moisture-stress history. This implies that the specified concrete strength (for example 6000 psi at the time of pre-stressing for the Fort St. Vrain pressure vessel) based on the testing of cylindrical specimens cured for a relatively limited amount of time may not reflect the true state of the pressure vessel concrete. If in fact the long term changes that can occur due to the environment lead to strength increases, then the specified concrete strength would be conservative. If on the other hand the net effect of the environmental factors operating on the concrete, including abnormal conditions, tends to weaken the concrete the margin of safety would be reduced. The following example of how this would operate is taken from the Fort St. Vrain FSAR[5-6]. The concrete at the vessel midheight is under an average circumferential prestress of about 1950 psi. It is assumed that the long term concrete strength is 60% of the specified strength at prestressing, or 0.6 x 6000 = 3600 psi. With this concrete strength it can be shown that nearly half the wall thickness (~4 ft) could lose all of its strength before the wall would collapse under the pre-stress load. A postulated loss of cooling water accident results in a maximum of less than 20" of concrete heated to >250°F. Even if all the strength in this section were lost, according to the analysis, the remaining thickness exceeds the minimum required by ~2 1/2 ft. The presumed conservatism in this analysis, as far as the properties of concrete are concerned, lie with the assumption that the concrete has lost 40% of its specified strength after the reactor has been operational for some long period of time. It is conceivable on the one hand that considerable volumes of the concrete have continued to increase in strength and are actually stronger than the specified strength at pre-stressing. It is also conceivable, especially in a loss of coolant accident, that appreciable volumes of concrete can be weaker than the estimates made in the cited FSAR. This will be discussed later.

Another consideration is that the specified concrete strength of the PCRV is actually not achieved. This could arise from the different curing conditions experienced by test cylinders and the massive concrete. The possibility for significant temperature increases due to the heat of hydration of the cement, coupled with the essentially sealed state of the massive concrete could lead to a weaker concrete. However, specimens cored from PCRV side walls after curing for $\sim$60 days were about 20% stronger than results from the trial mix[5-7]. The mix temperature for the PCRV was 45°F to compensate in part for the temperature rise on hydration. It appears that based on these measurements and the discussion in the earlier progress report (BNL 19763) the specified strength can be achieved in massive PCRV sections.

It was assumed earlier in the Fort St. Vrain FSAR that the concrete had deteriorated to effectively 60% of its specified compressive strength. There are very few factors that, under normal operating conditions, could cause such a reduction. Long times in the presence of moisture can result in additional hydration and strength increases for a number of years, depending on the cement composition and surface area[5-8]. Studies for the Fort St. Vrain pressure vessel have shown that for sealed concrete there is very little gain in strength after $\sim$4 months. Moist cured concrete of the same composition shows about a 5% increase in strength between 4 and 8 months[5-9]. This is about half the increase demonstrated by a concrete made with cement of half the surface as part of a long term study[5-8]. If this relation holds one might expect that for regions of the structure that are moist cured, i.e. have continuous access to water, the strength would continue to increase at most for 2-5 years, at a very slow rate. The effect of elevated temperatures would also tend to increase hydration rates, so it is likely that for this concrete there will not be much gain in strength due to hydration after ~8 months to one year.

The effect of temperature on the properties of concrete must be considered in more detail. Two temperature effects are distinguished: the effects due to the removal of the various free and bound waters when concrete is permitted to dry, and the effect of heat on chemical reactions and phase changes that can occur when concrete is heated in a sealed condition.

Under normal operating conditions the concrete is in contact with the PCRV liner at an average sidewall temperature of 150°F (for the Fort St. Vrain reactor), and is at ambient temperature at the outer wall about 9 ft away. The effect of this temperature distribution is to drive moisture from the hot to cooler regions, effectively drying the first foot or two around the liner, saturating a large region in the interior of the structure, and then the concentration decreases near the surface to an equilibrium value. The extent of hot face drying is of course a function of time, temperature, and the permeability of the concrete. For a hot face temperature of 257°F the drying depth is about 0.5 meters for 2 1/2 years; at 302°F the drying depth is about 1 meter in the same time[5-10]. The properties of dry concrete in this temperature region have been extensively investigated. There is essentially no strength decreases to these temperatures[5-11]. For a hot face temperature of 270°F and a temperature gradient of ~22°F/ft, the saturated concrete starts at a temperature of ~225°F (107°C)[5-10], which is above temperatures where hydrothermal reactions involving cement and concrete can take place[5-12]. If it is assumed that the lowest temperature at which hydrothermal reactions can take place is 140°F (60°C)[5-12], there would be a zone about 4 ft thick starting from the dry concrete boundary, of concrete that can undergo hydrothermal changes. Surrounding this zone is a third region of partially dried concrete extending to the outer surface. This simple analysis indicates that there can be three quite distinct regions within the concrete pressure vessel: a hot, dry region (Region I); a hot-to-warm, saturated region (Region II) where hydrothermal reactions can take place; and a cooler, partially dry-to-dry outer region (Region III).

There have been many studies of the strength of hot, dry concrete. In general there is little or no strength decrease to 400-500°F, tested hot. Cooling and testing at room temperature can lead to strength decreases. However, heating sealed concrete at 175°F (80°C) for 24 hours and testing at temperature gave compressive strength decreases to 85% of reference value and about 75% at 250°F. At 500°F the strength was less than 50% of the reference value, according to Lankard et al.[5-1]. Imlach and Taylor[5-13] studied the strength of sealed pastes at 285°F-300°F for 2 1/2-4 months. They observed strength decreases as much as 60% that resulted from the hydrothermal treatment. However, with the use of siliceous aggregates the compressive strength can become greater than the control strength.

The effects of very long times (i.e. years) at relatively low temperatures on the strength of sealed (Region II) concrete is an area about which very little is known. The extensive hydrothermal studies that have been done on cements and concretes are generally at much higher temperatures where the reactions are completed in a few hours or days$^{5-12}$. In view of the rather large volume of concrete that is potentially sensitive to strength degradation via hydrothermal reactions, this aspect of concrete technology must be scrutinized more closely.

In light of this possible mechanism of strength loss, the assumption discussed earlier, made in the Fort St. Vrain FSAR that the long term concrete strength may be 60% of the specified strength, may not be unreasonable$^{5-6}$.

The effect of stress on strength under temperature has been considered by some investigators and it appears that stressed concrete (compressive to 55% control strength) retains higher strengths when heated to 400°F and higher, than does unstressed$^{5-14}$. No information appears to be available on the effect of stress on heating sealed concrete.

The effect of an accident such as a loss of liner cooling water would cause a temperature increase and consequent change in the temperature gradient which could persist for some days. The volume of Region I concrete (hot-dry) would increase, the hot end of Region II would dry, and the cool end would encroach on former Region III concrete. These changes are shown schematically in Figure 5-13 along with a schematic illustration of possible changes to the strength of concrete. At present this picture is quite speculative, but derives from three facts: most of the concrete is effectively sealed so that

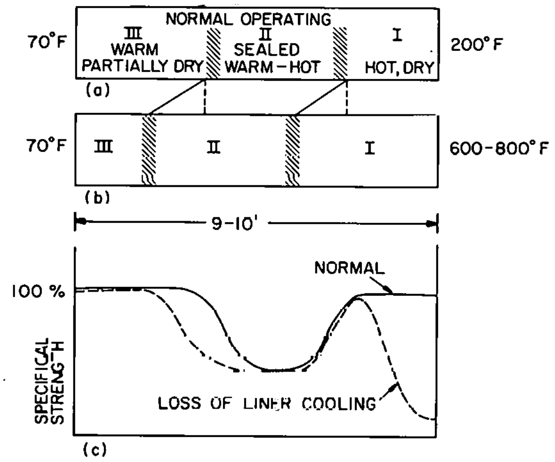

Figure 5-13a. Distribution of concrete zones I, II, III in normal operation.

Figure 5-13b. Redistribution of zones I, II, III after loss of liner cooling accident.

Figure 5-13c. Possible schematic distribution of strength before and after loss of cooling accident.

drying will not take place; the temperature of the sealed concrete is, in normal operation, at a temperature where hydrothermal reactions can occur; measurements of the effect of hydrothermal reactions on the compressive strength of cured concrete show significant reductions in strength. This appears to be an important area for further, more detailed study.

2

References

5-1. Lankard, D. R., Birkimer, D. L., Fondriest, F. F., and Snyder, M. J. Effects of Moisture Content on the Structural Properties of Portland Cement Concrete Exposed to Temperatures up to 500°F. ACI Publication SP 25, pp. 59-102.

5-2. Powers, T. C. Structure and Physical Properties of Hardened Cement Paste. J. Amer. Ceram. Soc. 41, 1-16 (1958).

5-3. Ganham, D. E. Low Slump Concrete Results in Cost Savings for Prestressed Containment Structures. J. Amer. Concrete Soc. 3, 126-29 (1974).

5-4. Wang, C. H. Creep of Concrete at Elevated Temperatures. ACI Publication SP 27, pp. 387-400, 1971.

5-5. Zielinski, J. L. and Sadowski, A. The Influence of Moisture Content on the Creep of Concrete at Elevated Temperatures. Preprints of the 2nd Intern. Conf. on Structural Mechanics in Reactor Technology, Vol. 3, Paper H6/3, Brussels, 1973.

5-6. Fort St. Vrain Nuclear Generating Station, Final Safety Analysis Report, Vol. IV, pp. D.2-18, Public Service Company of Colorado, Denver, Colorado.

5-7. Ibid., pp. E.16-2.

5-8. Washa, G. W. and Wendt, K. F. Fifty Year Properties of Concrete. ACI Journal Proceedings 72, 20-28, 1975.

5-9. Ref. 5-7, Figure E.16-2.

5-10. England, G. L. and Ross, A. D. Shrinkage, Moisture, and Pore Pressures in Heated Concrete. Paper SP 34-42 in Concrete for

Nuclear Reactors, Special Publication SP-34, American Concrete Institute, Detroit, Michigan, pp. 883-907, 1972.

5-11. See for example *Temperature and Concrete*, Publication SP-25, The American Concrete Institute, Detroit, Michigan, 1971.

5-12. Lea, F. M. *The Chemistry of Cement and Concrete*. Edward Arnold, Ltd., Glasgow, p. 188, 1970.

5-13. Imlach, B. V. and Taylor, H. F. W. Prolonged Hydrothermal Treatment of Cement Mixes. Trans. and J. Brit. Ceram. Soc. *71*(3), 71-75 (1972).

5-14. Abrams, M. S. Ref. 5-11, p. 33.

VI. Instrumentation and Monitoring (G. Bennett)

Bids have been received and are being reviewed regarding the mass spectrometer for Fort St. Vrain. This unit will incorporate a high resolution (500) mass analyzer, noble gas ion pumps and a detection system consisting of a rotating beam shutter and phase lock amplifier. Sensitivities of $\leqslant$ 10 ppmv will be possible for the species H_2, H_3, D_2, H_2O, N_2, O_2, CO, CO_2 and others.

A purchase order has been placed for the gas chromatograph to be used in monitoring the circulating gas concentrations in the BNL test loop. The instrument ordered is the Varian Aerograph Model 1420 (dual column) with a thermal conductivity detector.

The gas calibration system to be used in qualifying the mass spectrometer system for Fort St. Vrain and the gas chromatograph for the BNL loop has been fabricated and is ready for initial tests.

IX. Phenomena Modeling and Systems Analysis

A. HTGR Safety Code Library

During the reporting period, conversion of the codes GAKIT and RECA has continued and work was begun on converting CORCON and SORS to the BNL CDC 7600 system. At the end of the quarter the BNL HTGR Safety Code Library received the transient analysis program TAP from General Atomic Company. Table 9-1 summarizes the status of the 29 programs currently being maintained in the library.

B. Conversion of CORCON (C. Sastre)

The tape containing CORCON (Archive No. S45D-1407) and input for a sample problem has been received from General Atomic Company (GA). The program has been converted to the BNL CDC 7600 computer and it now compiles and executes. The task of conversion verification is hampered by the lack of a consistent set of input and output. This is expected to be obtained at the end of June. In addition to the usual translation from FORTRAN V to FORTRAN IV, the conversion has involved some variable initializations in order to avoid the generation of indefinites during the first iteration. This was necessary because of differences in the way the Univac 1108 and the CDC 7600 handle indefinite conditions. It was also necessary to include a renormalization of the power distributions to avoid accumulation of round-off errors that led to improper heat balances.

The main effort to date on the study of CORCON has been the tracing of the program to understand in detail the method of solution and the assumptions and data implicit in it.

Table 9-1

HTGR Safety Code Library

Program	Status	Proprietary	Function
CRECT	OP	NP	Corrects data on ENDF/B tape.
LISTFC	OP	NP	Lists data from ENDF/B tape.
RIGEL	OP	NP	Manipulates data on ENDF/B tape.
ENDFB2	OP	NP	Converts data on ENDF/B tape to binary.
FLANGE		NP	Prepares thermal cross section transfer arrays.
GAND2	OP	NP	Prepares fine group fast, resonance, and thermal cross sections from ENDFB2 binary tapes.
GFE2	OP	NP	Prepares fine group fast cross sections from ENDFB2 binary tapes.
MAKE	OP	NP	Prepares fine group fast cross section tape from GFE2 for spectrum codes.
WTFG	OP	NP	Prepares fine group thermal cross section tape from GAND2 or FLANGE for spectrum codes.
PRINT	OP	NP	Reads the fast cross section tape produced by MAKE.
SPRINT	OP	NP	Reads the thermal cross section tape produced by WTFG.
GGC4	OP	NP	Prepares broad group cross sections from MAKE and WTFG tapes.

C = In the process of being converted to the CDC-7600.
OP = Operational on the BNL CDC-7600 system under Scope 2.
R = Recently received from General Atomic Co. or Argonne Code Center.
P = General Atomic Company proprietary code.
NP = Not considered to be a proprietary code.

Table 9-1 - Cont'd.

Program	Status	Proprietary	Function
INTERP	OP	NP	Prepares broad group cross sections from MICROX output data tapes.
IDX	OP	NP	Performs one-dimensional, diffusion theory, steady-state calculations.
FEVER-7	OP	NP	Performs one dimensional, diffusion theory, burnup and reload calculations.
TEMCO-7	OP	NP	Computes reactor temperature coefficients from input cross section data.
BLOOST-7	OP	NP	Performs zero-dimensional reactor kinetics calculations.
GAKIT	C	NP	Performs one-dimensional reactor kinetics calculations.
TWIGL	OP	NP	Performs two-dimensional light-water reactor kinetics calculations.
TAC-2D	OP	NP	Performs two-dimensional, transient conduction analyses.
FLAC	OP	NP	Calculates steady-state flow distributions in arbitrary networks with heat addition.
POKE	OP	P	Calculates steady-state flow distribution and fuel and coolant temperatures in a gas-cooled reactor.
RECA	C	P	Calculates time-dependent flow distribution and fuel and coolant temperatures in the primary system.
CORCON	C	P	Computes the temperature history and fission product redistribution following a loss of all convective cooling of the core.

Table 9-1 - Cont'd.

Program	Status	Proprietary	Function
SORSG	C	P	Computes the release of volatile and non-gaseous fission products from an HTGR core during thermal transients.
GOPTWO	OP	NP	Analyzes the steady state graphite burnoff and the primary circuit levels of impurities.
OXIDE-3	OP	P	Analyzes the transient response of the HTGR fuel and moderator to an oxidizing environment.
SAMPLE	OP	NP	Propagates uncertainties in probability distributions by Monte Carlo technique.
TAP	R	P	Calculates the transient behavior of the integrated HTGR power plant.

The code calculates the temperatures in the core, reflector and thermal insulation of the main primary system cavity as a function of time following a non-mechanistic depressurization accident with a complete loss of helium cooling capability. The only heat sink assumed is that of the cooling coils of the liner. Heat is assumed to be transferred through the core by conduction only. Heat is transferred from the top reflector and core support blocks to the thermal insulation of the upper and lower plena by radiation. The heat source (natural decay of fission products) is represented by 5 families or groups with different properties whose migration through the core is used to adjust the heat source term in the temperature distribution calculation. The migration of fission products is assumed to be driven by a gas current which transports the products upwards. Deposition by condensation is assumed in the colder region. This gas flow does not result in transfer of heat. This assumption leads to higher computed temperatures in the core and hence higher releases of fission products. However, the neglect of convection currents might lead to an underestimate of the upper plenum surface temperatures.

C. Effects of Water Ingress Utilizing GOPTWO (L. Epel)

The GOPTWO computer program was used extensively during the quarter to investigate the steady state concentrations of water vapor in the HTGR for various water ingress rates. This was done over a wide range of ingress rates (0.01 to 100 pounds per hour) and for a number of different graphite-water reaction rates. The details are recorded in an internal memorandum (Reference 9-1).

The GOPTWO program computes the steady state concentrations of H_2O, H_2, CO, and CO_2 resulting from the following reactions:

$$C + H_2O \rightarrow CO + H_2$$

$$CO + H_2O \rightleftarrows CO_2 + H_2$$

$$C + CO_2 \rightarrow 2\ CO$$

The code assumes that the rates for these reactions are governed by Hinshelwood type equations for the thermally-induced reactions. A supplementary, temperature dependent, radiation-induced reaction rate is also taken into account if desired by the user. GOPTWO considers the physical situation in which there is an upper plenum, a graphite core composed of parallel channels, a lower plenum, and a gas purification system. The code simulates the flow of the mixture of gases from the upper plenum, through the parallel channels (each channel has a unique flow rate and axial temperature profile), to the lower plenum where mixing occurs. GOPTWO then accounts for purification of the gas and the addition of water to the mixture before returning the gases to the upper plenum and repeating the cycle. When the change in concentration of the various gases in the mixture is insignificant at all locations in the helium circuit, the steady state solution is at hand.

The input to the code allows the user to choose rate constants for the thermally-induced chemical reactions, temperature dependent diffusion coefficients for gases in graphite, radiation-induced chemical reaction rate constants, flow distributions through parallel channels, axial temperature profiles for the parallel flow channels, and geometric and physical parameters for the reactor system as well as the purification and ingress rates.

The main purpose of the study was to determine whether or not the core support posts might be afforded any protection from the corrosive effects of steam existing in the upper plenum by the hot core graphite. Therefore, the upper range of graphite-steam reaction rates to be found in the literature, as well as high values of the diffusion coefficient were used. Specifically, the reaction rate utilized for the graphite-steam reaction is one that is due to Barsell (Reference 9-2) and is 75% higher than the one used in the OXIDE-3 code. If F is the fraction of graphite reacting per hour, the homogeneous reaction rate described in this reference is:

$$F = \frac{1.868 \times 10^{8} \exp(-40{,}900/RT)\, P_{H_2O}}{1 + .0166 \exp(28{,}600/RT)\, P_{H_2}{}^{.75} + .0531 \exp(27{,}500/RT)\, P_{H_2O}}$$

where the temperatures are in degrees Kelvin, the partial pressures are in atmospheres, and R = 1.986 calories/mole Kelvin. Similarly, the diffusion coefficient of steam in graphite was chosen from the upper range of reasonable values:

$$D = 1.06 \times 10^{-6} \frac{T^{1.58}}{P}$$

where the diffusion coefficient is in cm^2/sec, the temperature is in degrees Rankine, and the partial pressure of steam is in atmospheres.

Using the Fulton Generating Station as a model, it was found that at steady state, the concentration of steam in the lower plenum did not differ appreciably from the concentration in the upper plenum, regardless of ingress rate, for typical operating conditions. In fact, when the graphite-steam reaction rate was subsequently arbitrarily increased by a factor of ten, the depletion of steam from the helium by the core graphite was still almost negligible.

An interesting artifact of the calculations was the simple relationship between steady state steam concentration and water ingress rate for the assumed operating conditions:

$$C_s \text{ (psia)} = 5.32 \times 10^{-3} L^{1.313}$$

where the leak rate is in pounds per hour. The above relationship held closely for $0.01 < L < 100$. Similarly, the carbon monoxide (and hydrogen) concentrations could reasonably be approximated over most of the ingress range by:

$$C_{cm} \text{ (psia)} = 0.073 L^{0.967}$$

A useful relationship, between carbon monoxide concentration and water vapor concentration, is easily derived from the above two expressions by eliminating the ingress rate:

$$C_{cm} = 3.48 C_s^{0.736}$$

where the concentrations are expressed in psia.

Finally, a comparison was made of the steady state solution from GOPTWO with an OXIDE-3 run to steady state. The parameters in GOPTWO and OXIDE-3 that are adjustable by the user during code input preparation were made as consistent with each other as possible. The GOPTWO results agreed with the OXIDE-3 results within about 20% under these conditions.

D. <u>OXIDE-3</u> (J. Skalyo)

In the January-March, 1975 Quarterly Report, BNL 50450, it was noted that it was necessary to properly differentiate between different versions of the OXIDE-3 program because of the changes which have been made in the code during its evolution. A new Fortran listing of the OXIDE-3 code was obtained from GA during this quarter with an attendant input and output of a sample problem. The introduction of a new afterheat calculation by GA for post trip times less than 22 seconds (not 25 seconds as stated in Amendment 1 of GA-LTR-7) was verified and incorporated into the BNL version of the code. A comparison of the Univac 1108 output for the sample problem was then made with results generated by the BNL CDC 7600 and excellent agreement was noted.

This agreement of results extended also to the release of Cs and Sr into the coolant stream; it was noted in BNL 50450 that these results were particularly variable and hence suspect. A. Bowman (LASL) has since then pointed out that the current version is in error in this part of the calculation and the appropriate correction will be incorporated into the code.

OXIDE-3 is currently being used at BNL for the calculation of equilibrium impurity concentrations in the primary coolant stream resulting from different constant steam leak rates while the HTGR operates at full power. The calculated impurity conditions in the primary coolant stream will serve as scoping data for the design of an experiment to study the effects of oxidation on core support post graphite. Parameter sensitivity studies are important in this regard and have been initiated so that priority can be established on an experimental program to determine an evidentiary graphite data base for the HTGR reference design. It is important here to verify that the limit of 10 ppmv of oxidant and the possible existence of localized catalytic attack on some of the core support posts will not have an adverse effect on reactor safety.

OXIDE-3, as written, is basically meant for short time transient calculations. For steady state calculations, we have additionally obtained the GOPTWO oxidation code, developed at Battelle Pacific Northwest Laboratory from W. C. Morgan. While GOPTWO is written to efficiently solve the equilibrium problem, it was thought that some calculations to steady state should be done using OXIDE-3 for purposes of comparison.

OXIDE-3 is written so that the time step for the calculation is fixed in each of six time regions extending over the entirety of the transient. This is not a feasible method for running OXIDE-3 in a calculation to equilibrium which requires following a time history of approximately 100k-200k seconds (the longest physical time constant in the problem is the purification process, 36k seconds). The program has therefore been modified at BNL to include a variable time step feature which adjusts the time step throughout the transient while also assuring the absence of numerical oscillations in the solution. Additionally, a maximum time step feature has been included to satisfy limits imposed by various time constants involved in the program (diffusion, reaction, purification, etc.). This latter feature is being further investigated in order to fully justify the use of OXIDE-3 for steady state calculations.

The calculations which are described below are meant to be illustrative in nature and are directly related to the sample problem shown in Section 9 of GA-LTR-7 for a 3000 MW reactor. The input for the present calculations are therefore not repeated here. The main differences between Section 9 and what follows are that here the time step is automatically varied, the reactor is not scrammed, a step function steam leak rate is started at t = 0, the helium cold-leg temperature is fixed at T = 640°F, and the helium flow rate is fixed at 3066 lb/sec (the latter three parameters are shown as Tables 1, 2, and 3 on page 9-9 in GA-LTR-7).

In the first series of three calculations the steam leak rate is fixed at 0.009, 0.09, and 0.9 lb/h, respectively. For the case of L = 0.09 lb/h, (a value that gives 10 ppmv of oxidant), the partial pressure of steam (psia) in the upper and lower plenums is accurately given for $0 < t < 200{,}000$ by

$$P_{upper} = [3.50 - 2.29 \exp(-0.0072\ t) - 1.17 \exp(-0.000025\ t)] \times 10^{4}$$

$$P_{lower} = [3.49 - 2.28 \exp(-0.0070\ t) - 1.17 \exp(-0.000025\ t)] \times 10^{-4}$$

where t is in seconds. The formulas are non-linear least squares fits to the numerically calculated time dependence. The upper and lower plena are subjected to the same pressure to within the standard deviations associated with the fits (the neglect of a pressure drop across the core is built into the code). This equality is not surprising when one considers that the helium circulation time is ~6 seconds compared with an estimated diffusion time constant of ~100 seconds (this estimate is based on one dimensional diffusion of steam from the coolant channel surface to the fuel stick center at a temperature of 1650°F). The hydrogen and carbon monoxide partial pressure-time dependences are given by

$$P_H = [6.68 + 0.0682 \exp(-0.00138\ t) - 6.75 \exp(-0.000016\ t)] \times 10^{-3}$$

$$P_{CO} = [6.67 + 0.167 \exp(-0.00052\ t) - 6.85 \exp(-0.000021\ t)] \times 10^{-3}$$

where the partial pressures are in psia.

The results for all three leak rates are illustrated in Figures 9.1-9.4 for steam, hydrogen, carbon monoxide, and the CO/H_2O ratio, respectively. Note that the scale multipliers are for Figures 9.1-9.3 only. The deviation from a linear dependence on the leak rate is clearly evidenced. The dependence of the equilibrium partial pressure of steam on the leak rate (in pounds per hour) is

$$P_{St}\ (\text{psia}) \approx 0.0064\ L^{1.18}$$

which compares favorably with the GOPTWO results.

The second series of calculations varied the graphite-steam reaction rate at a fixed steam leak of 0.09 lb/h. The Langmuir-Hinshelwood equation for the reaction rate (Eq. 3-33 of GA-LTR-7) has been multiplied by a factor F with values 100, 1, and 0.01 for this series. These results are shown in Figures 9.5-9.8 for steam, hydrogen, carbon monoxide, and the CO/H_2O ratio, respectively (note there are no scale multipliers on these curves).

It is noted that the OXIDE-3 sample problem multiplies the fuel rod reaction rate by an additional factor of 10 (supplied as input). This factor is also used in the present series. For the case where the graphite-steam reaction rate is multiplied by 0.01,

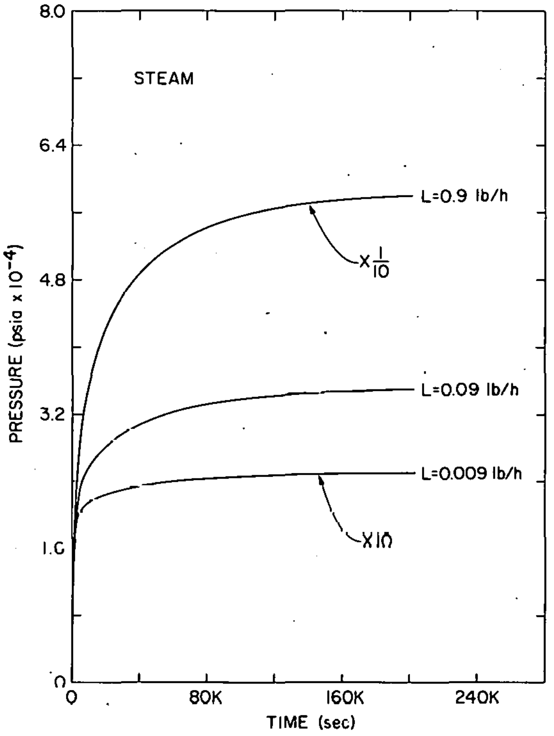

Figure 9-1. Partial pressure of steam in the hot plenum as a function of time due to various step function leak rates L starting at t = 0.

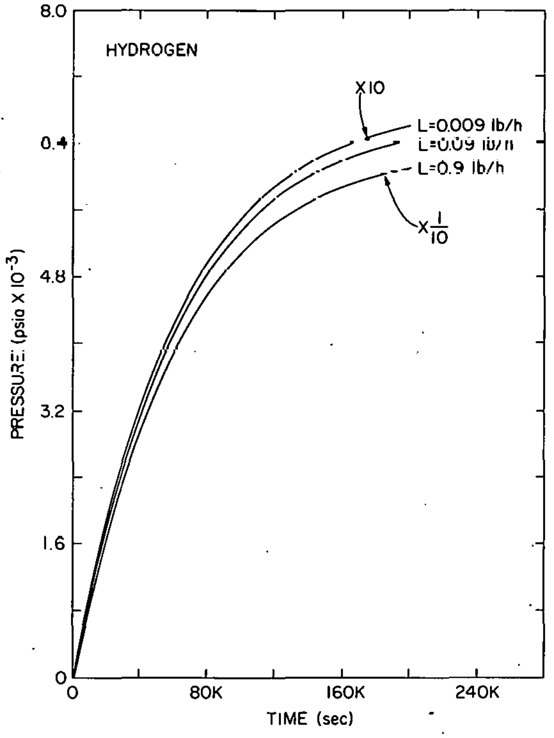

Figure 9-2. Partial pressure of hydrogen in the hot plenum as per Figure 9-1.

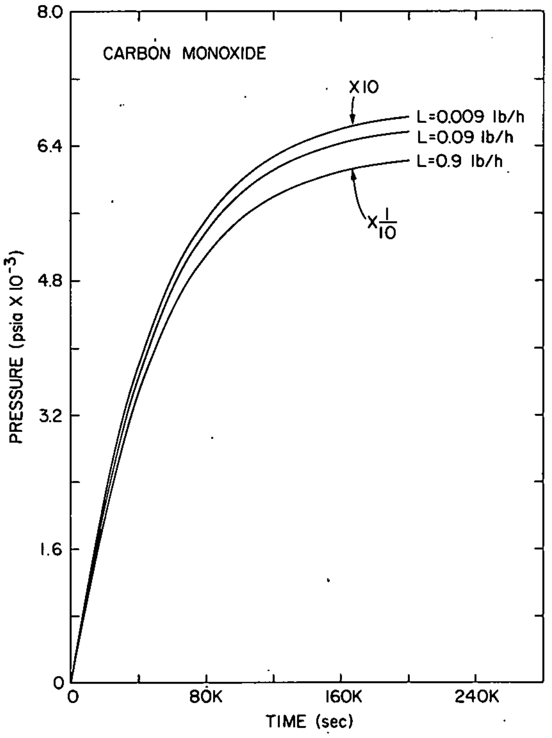

Figure 9-3. Partial pressure of carbon monoxide in the hot plenum as per Figure 9-1.

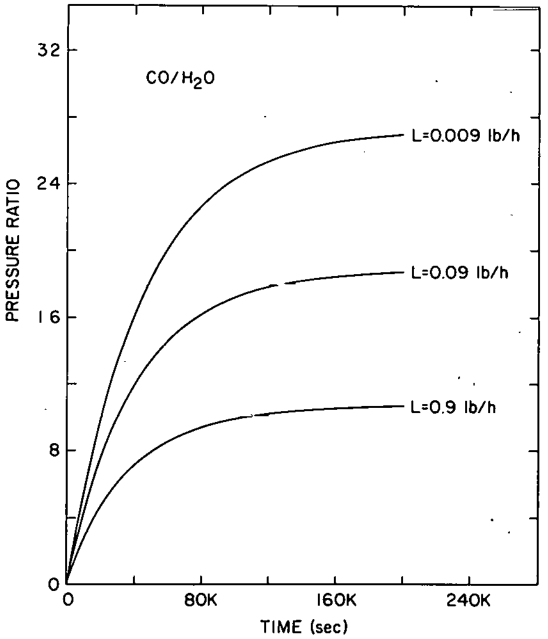

Figure 9-4. The ratio of the partial pressures of carbon monoxide and steam in the hot plenum as per Figure 9-1.

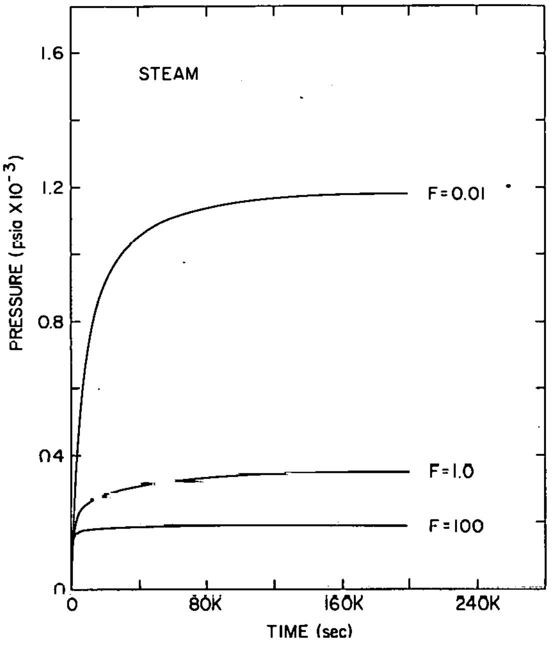

Figure 9-5. Partial pressure of steam in the hot plenum as a function of time due to a step function leak rate L = 0.09 lb/h for various graphite-steam reaction rate multipliers F.

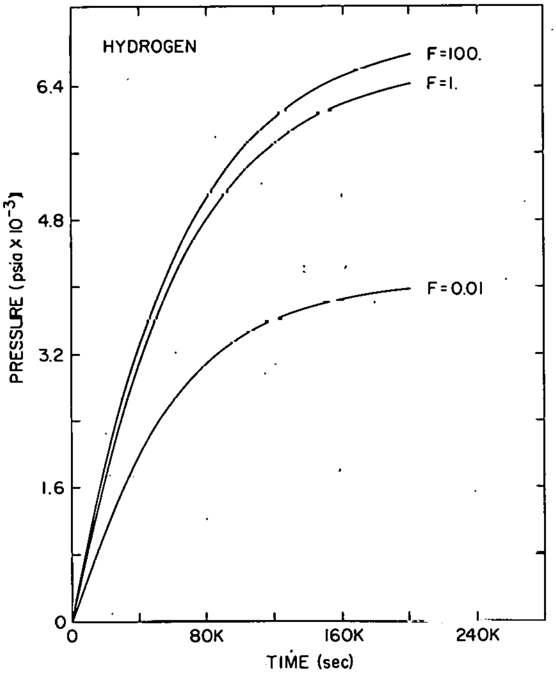

Figure 9-6. Partial pressure of hydrogen in the hot plenum as per Figure 9-5.

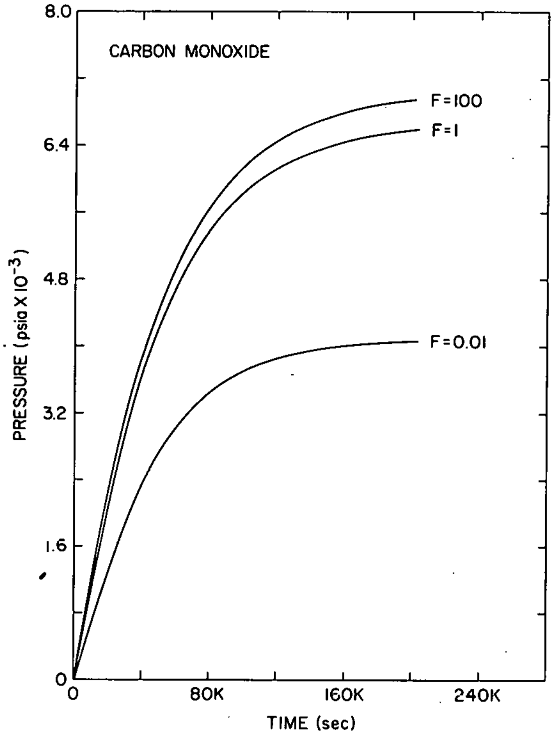

Figure 9-7. Partial pressure of carbon monoxide in the hot plenum as per Figure 9-5.

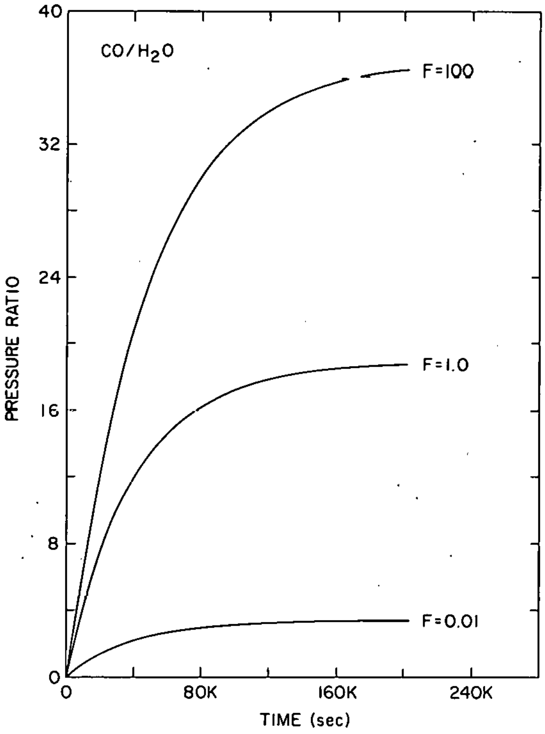

Figure 9-8. The ratio of the partial pressures of carbon monoxide and steam in the hot plenum as per Figure 9-5.

it was apparent that an appreciable fuel hydrolysis is taking place. It is not clear at this time whether the factor of 10 for the fuel rod graphite reaction is therefore always a conservative approach, since its use tends to result in an underestimate of fuel hydrolysis.

It is appropriate that a simplified model that justifies the use of the two exponential terms in fitting the time dependences be presented here. The simplest model is one which consideres three volumes: a coolant volume, the web graphite pore volume, and the fuel rod graphite pore volume. For further simplification, the latter two volumes can be grouped together since our interest here centers on the steam concentration in the coolant volume. Thus the distinction between the fuel graphite and web graphite with respect to reaction rate differences and hydrolysis effects are lost. The validity of the two-volume model is upheld by the numerical results of the OXIDE-3 calculations for steam concentration which were fitted very well by two exponential terms. (Since the three-volume model results in three exponential terms it is not clear that the additional complexity is justified at this time). Furthermore, only the steam is considered in this analysis, since the carbon monoxide and hydrogen concentrations are easily determined once the steam concentration is known. It is noted that in the two-volume model the carbon monoxide and hydrogen concentrations have solutions involving four exponential terms. Here, it is doubtful that anything could be gained by complicating the numerical analysis beyond the two term solution since additional terms contribute negligibly to an already excellent fit.

We let C be the number of moles of steam, L is the molar leak rate of steam, K_1 is the fraction of the coolant inventory purified per unit time, K_2 is the fraction diffusing per unit time from the coolant volume to the pore volume, and K_3 is the fraction reacting to CO and H_2 per unit time. The equation for the coolant volume can be written as:

$$\dot{C}_c = L - K_1C_c - K_2R\left[C_c\,\frac{1}{\frac{V_1}{T_1}+\frac{V_2}{T_2}} - C_p\left(\frac{\tilde{T}_p}{V_p}\right)\right]$$

and that for the pore volume as:

$$\dot{C}_p = K_2R\left[C_c\,\frac{1}{\frac{V_1}{T_1}+\frac{V_2}{T_2}} - C_p\left(\frac{\tilde{T}_p}{V_p}\right)\right] - K_3C_p.$$

The subscripts c and p refer to the coolant or pore volume, respectively, R is the gas constant, $\frac{V_1}{T_1}$ and $\frac{V_2}{T_2}$ are the volume divided by temperature calculated for plenum 1 (hot leg) and plenum 2 (cold leg), respectively, and $\left(\frac{\tilde{T}_p}{V_p}\right)$ is some suitable average over the pore volume. Substituting

$$D = \frac{d}{dt},\ \alpha_1 = K_2R\,\frac{1}{\frac{V_1}{T_1}+\frac{V_2}{T_2}},\ \text{and}\ \alpha_2 = K_2R\left(\frac{\tilde{T}}{V}\right),$$

one obtains

$$\begin{pmatrix} D + K_1 + \alpha_1 & -\alpha_2 \\ -\alpha_1 & D + \alpha_2 + K_3 \end{pmatrix} \begin{matrix} C_c \\ C_p \end{matrix} = \begin{pmatrix} L \\ 0 \end{pmatrix}$$

The solution is

$$C_c = A_c e^{m_1 t} + B_c e^{m_1 t} + \frac{(\alpha_2 + K_3)\,L}{K_3K_1 + K_3\alpha_1 + K_1\alpha_2}$$

$$C_p = A_p e^{m_1 t} + B_p e^{m_2 t} + \frac{\alpha_1 L}{K_3 K_1 + K_3 \alpha_1 + K_1 \alpha_2}$$

where $m_{1,2}$ are the solutions of the qudaratic

$$m^2 + (K_1 + K_3 + \alpha_1 + \alpha_2)m + K_3 K_1 + K_3 \alpha_1 + K_1 \alpha_2 = 0$$

and A_c, B_c, A_p, and B_p are integration constants related by the differential equations (the determinant is quadratic in D, hence only two independent integration constants are obtained).

Note the linear relation of the equilibrium concentration to the leak rate. The observed deviation (from linear) obtained from the OXIDE-3 calculation is, of course, due to the more complicated form of the Langmuir-Hinshelwood reaction rate; i.e. K_3 is not really constant. While it is not meant to read too much into the above formulation, it may be that the good fit obtained to the numerical data by this form is due to the dominance of the constant term in a Laguerre polynomial expansion of a more exact solution.

When the concentration of carbon monoxide is also calculated, this model gives the conservation relation:

$$L = K_1 (C_{steam} + C_{CO})$$

which holds for the coolant volume at equilibrium (in the absence of fuel hydrolysis). The OXIDE-3 code does not take account of any gaseous products resulting from the hydrolysis. This is justifiable since the number of moles of hydrogen resulting therefrom is negligible compared with that resulting from the graphite-steam reaction when the rate equations are as given in GA-LTR-7.

E. Component Modeling - Turbo Compressor (L. Epel)

The model of the helium compressor and its steam turbine driver that was incorporated into the TFR program (see previous Quarterly Progress Report) has been made into a "free standing" code so that the characteristics of the compressor-turbine combination could be tested and so that the package could be exported to any user who wishes to utilize this module*. A complete report on this code, SSTHC (Series Steam Turbine Helium Circulator), has been written and describes the mathematical model, the manner in which the actual compressor and turbine characteristics are simulated, and the handling of the thermodynamic properties of both helium and steam/water (Reference 9-3). In addition, the report describes the thirteen subroutines in SSTHC, it presents a listing of the program, and it includes a sample problem input and output.

At the discretion of the user, either ideal gas or real gas properties can be utilized in the code, for both helium and steam. The cost of using real gas properties is incurred in computer running time, of course.

The heart of SSTHC is the three subroutines COMPRES, TURBIN, and POUT. The first of these computes the compressor pressure ratio and compressor efficiency given inlet flow rate, inlet helium conditions, and machine speed. The compressor performance characteristics obtained from GA were fit by least squares techniques to yield poly-

---

*One request for this package has already been received from the Division of Technical Review, Office of Nuclear Reactor Regulation, NRC.

nomial expressions for the dependent variable in terms of the reduced flow rate. Similarly, polynomial expressions were derived for the turbine parameters. These approximations were compared to the original data supplied by GA and generally agreed to within a percent. For the turbine, however, the isentropic enthalpy change appears in the independent as well as dependent variable and hence an iterative scheme must be used in TURBIN to extricate this quantity. The result of this subroutine yields the exit enthalpy, the turbine efficiency, and the turbine power. Subroutine POUT computes the turbine exit pressure and temperature, given inlet conditions and the efficiency and exit enthalpy from TURBIN. The other subroutines in SSTHC handle thermodynamic properties of helium and steam, read input and write output, or perform service calculations (such as computing flow resistance, interpolating in various tables, etc.).

The program was run to demonstrate its operability. Starting with steady state operation of the turbo-compressor set, a ramp-down of turbine flow rate in conjunction with ramp-downs in turbine inlet and outlet pressures was simulated. This problem was repeated four times:

- in problem 1 real helium and real steam properties were used,
- in problem 2 ideal helium and ideal steam properties were used,
- in problem 3 ideal helium and real steam properties were used,

- in problem 4 real helium and real steam properties were used but the moment of inertia of the turbo-compressor wheel was halved (i.e. 7200 lb ft^2 rather than 14,400 lb ft^2).

Figure 9-9 indicates some results of these computations. For this particular problem it appears that the circulator speed variation with time is rather insensitive to the moment of inertia of the rotor assembly. A comparison of problem 1 with problem 2 and then with problem 3 indicates that although use of the ideal gas approximation for helium may be acceptable, this same approximation applied to steam can change the results appreciably.

F. Consolidated Plant Model (TFR)

The 22-volume representation of the HTGR primary and secondary systems described in the previous progress report was used in an attempt to simulate some simple plant transients. Numerical instabilities are still being encountered but they are no longer due to the turbo-compressor modeling. Rather, the problem seems to originate in the steam generators, probably because of the large change in thermodynamic properties that the steam side experiences coupled with the attempt to model these effects using a limited number of nodes in the steam generator. More attention will be directed toward this problem in the future.

In the meantime, this troublesome portion of the model has been side-stepped temporarily, by a judicious choice of sample problems, so that TFR could at least be tested under somewhat limited boundary

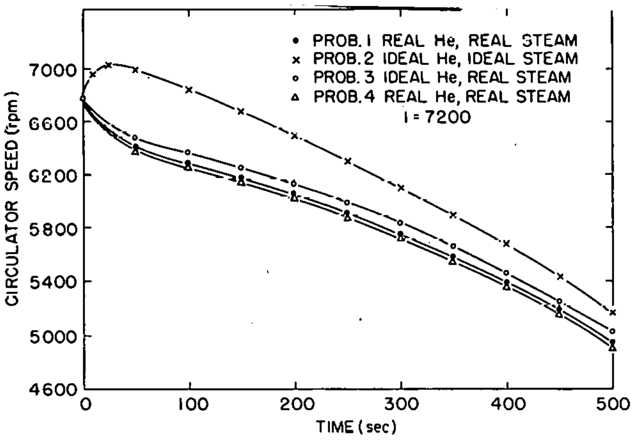

Figure 9-9. Circulator performance for rapid load decrease transients.

conditions. To illustrate TFR capabilities some sample problems were run in which the steam conditions to the compressor turbine were controlled independently of TFR predictions for the secondary loop.

The illustration shown here is a simple perturbation from steady state operation; the reactor power was ramped down linearly from 100% to 10% during the time interval from 1 to 2 seconds and then held constant at 10% for the remainder of the 200-second (reactor time) simulation. The steam generators for this case have been modeled as dumping the heat from the primary circuit in proportion to the helium-to-secondary temperature difference. The program appears to have behaved normally and Figures 9-10 through 9-13 represent some of the results of the calculation. It must be remembered that numerical values shown here are only representative of HTGR conditions; they should not be construed to be predictions of actual transient conditions. The fuel centerline temperature is seen to fall monotonically from just below 3200°F to under 1200°F at 200 seconds (Figure 9-10) and is still decreasing at the termination of the calculation. The lowering of the fuel temperature results in a decrease in the heat flux into the primary coolant (Figure 9-11) and a subsequent decrease in core exit temperature (Figure 9-12). Since the primary circuit is essentially at constant volume, the temperature decrease results in a pressure decrease from the design pressure to just below 500 psia at 200 seconds (Figure 9-13).

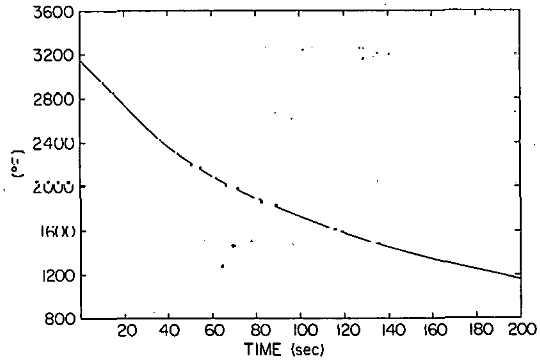

Figure 9-10. Fuel centerline temperature.

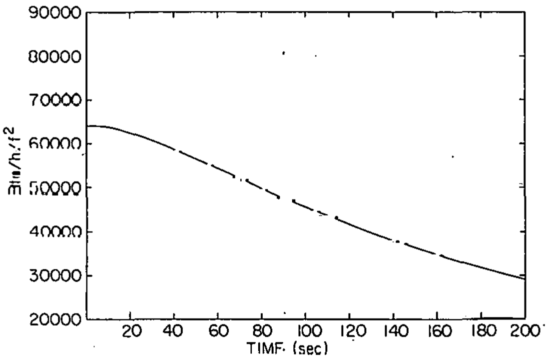

Figure 9-11. Heat flux into helium.

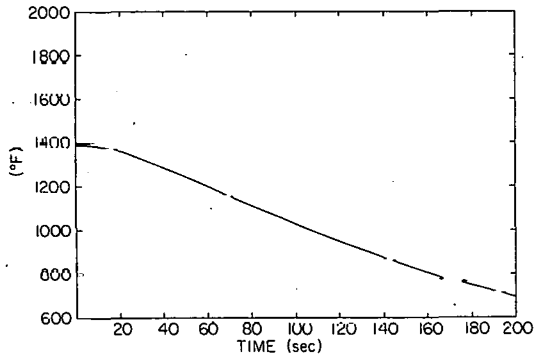

Figure 9-12. Core outlet helium temperature.

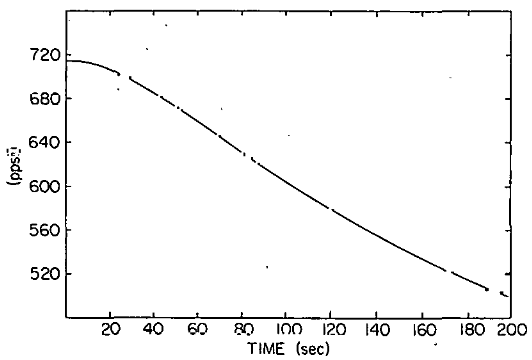

Figure 9-13. Average helium pressure in core.

Other sample problems have been run that involve power ramp-down with simultaneous compressor turbine steam flow and steam pressure ramp-down. The results of these simulations are being studied to determine if the code is behaving properly and will be detailed in subsequent reports.

The next improvement to TFR will be to provide the capability of separately controlling two steam generator/circulator loops. This will allow for the study of those transients in which all of the steam generator loops do not act in unison; e.g., isolation of one out of six steam generators due to tube failure.

References

9-1. Epel, L. G. Steam Concentration in Lower Plenum of HTGR, BNL Memorandum, May 23, 1975.

9-2. Monthly Progress Report for the GCR Programs at ORNL, GCR-74-32, October 1974.

9-3. Versteegen, P. L. and Sargis, D. A. SSTHC - A Program to Evaluate the Series Steam Turbine Helium Circulator Performance Under Dynamic Conditions, April 18, 1975.

X. Review of Group Activities

A. Safety Aspects of Hydrogen Cyanide in the HTGR (S. Nicolosi)

In the event of a depressurization accident of a High Temperature Gas Cooled Reactor (HTGR), a possibility exists for the generation of chemical poisons.

Various factors may contribute to this possibility such as the large surface area and the high heat capacity of the graphite core, the high operating temperature, various fission products which may act as catalysts, a possibility of both steam and air ingress, and the presence of radiation which may induce some reactions.

The potential production of hydrogen cyanide as the result of a steam ingress accident followed by a depressurization (air ingress) accident is under consideration. This analysis was based upon data from the accident analysis section of the General Atomic Standard Safety Analysis Report (Amendment 0). Prior to this analysis, an extensive literature search was conducted to examine as many of the syntheses of HCN as possible. The reactions considered in this study were:

$$\frac{3}{2}\,H_2 + CO + \frac{1}{2}\,N_2 = HCN + H_2O$$

$$\frac{1}{2}\,H_2 + C_{(graphite)} + \frac{1}{2}\,N_2 = HCN$$

$$H_2O + C_{(graphite)} = CO + H_2$$

The equilibrium HCN partial pressure resulting from the initial accident conditions described in GASSAR was obtained using the law of mass action. The expression was solved by Newton's iterative approximation method. The acceptable concentration of HCN (Merck Index of Chemicals and Drugs) is 10 ppmv. The calculation shows that if the reactor temperature is 2000°K or higher, the HCN concentration in the containment may reach 10 ppmv. At higher temperatures (3500°K) production is slightly increased. Details of this work are documented in an internal memorandum to file.

B. Combustible Gases and Explosion Hazards in the HTGR (C. Yang)

Steam and/or water may enter into the primary coolant system as a result of such incidents as: steam generator or helium circulator bearing water supply failures. The reaction between the steam and the core graphite produces hydrogen and carbon monoxide gases. If these gases leak into the containment building or if oxygen in the containment building leaks into the PCRV, an explosive mixture may be formed.

The integrity of the PCRV and/or the containment building may be impaired if an explosion is set off in these mixtures.

A conference to explore the consequences of the various combustion processes to the safety of the HTGR was held at BNL on the 1st and 2nd of July, 1975. Participants of the meeting included five visiting consultants: Abraham Berlad, Howard Palmer, Merwin Sibulkin, Roger Strehlow and Ching Yang.

The philosophy of the HTGR Safety Program and summary of the specific BNL program were introduced at the beginning of the meeting. Reactor environment and structural design considerations were presented. A general discussion of the various combustion processes such as homogeneous explosion, flame propagation, detonation, diffused flames and slow reactions in the reactor environment followed.

The production, accumulation, mixing and transport of combustible gases in the reactor were discussed.

It became quite clear that the conditions inside the reactor such as pressure, temperature and geometric configurations, etc. are vastly different from the ones under which general combustion experiments are performed in laboratories. A direct application of the measured flammability, explosion limits, and detonability limits may not be feasible. Specific conditions under which combustion hazards may occur must be assessed and delineated. The consultants have proposed a follow-up meeting in November to consider more specific problems and suggest special studies if necessary.